Materials Today Bio 23 (2023) 100866

Contents lists available at ScienceDirect

Materials Today Bio

journal homepage: www.journals.elsevier.com/materials-today-bio

Synergistic effect of hierarchical topographic structure on 3D-printed Titanium scaffold for enhanced coupling of osteogenesis and angiogenesis

Leyi Liu [a,b,1], Jie Wu [a,b,1], Shiyu Lv [a,b,1], Duoling Xu [a,b], Shujun Li [c], Wentao Hou [c], Chao Wang [a,b,*], Dongsheng Yu [a,b,**]

[a] Hospital of Stomatology, Sun Yat-sen University, Guangzhou, 510055, China
[b] Guangdong Provincial Key Laboratory of Stomatology, Guanghua School of Stomatology, Sun Yat-sen University, Guangzhou, 510055, China
[c] Institute of Metal Research, Chinese Academy of Sciences, Shenyang, 110016, China

ARTICLE INFO

Keywords:
Hierarchical topography
UiO-66
Coupling of osteogenesis and angiogenesis

ABSTRACT

The significance of the osteogenesis-angiogenesis relationship in the healing process of bone defects has been increasingly emphasized in recent academic research. Surface topography plays a crucial role in guiding cellular behaviors. Metal-organic framework (MOF) is an innovative biomaterial with nanoscale structural and topological features, enabling the modulation of scaffold physicochemical properties. This study involved the loading of varying quantities of UiO-66 nanocrystals onto alkali-heat treated 3D-printed titanium scaffolds, resulting in the formation of hierarchical micro/nano topography named UiO-66/AHTs. The physicochemical properties of these scaffolds were subsequently characterized. Furthermore, the impact of these scaffolds on the osteogenic potential of BMSCs, the angiogenic potential of HUVECs, and their intercellular communication were investigated. The findings of this study indicated that 1/2UiO-66/AHT outperformed other groups in terms of osteogenic and angiogenic induction, as well as in promoting intercellular crosstalk by enhancing paracrine effects. These results suggest a promising biomimetic hierarchical topography design that facilitates the coupling of osteogenesis and angiogenesis.

1. Introduction

The reconstruction of maxillofacial bone defects resulting from tumor excision, trauma, and congenital diseases continues to pose a significant challenge. Currently, the use of autologous bony-free flap implantation remains the preferred method for maxillofacial reconstruction [1]. However, this approach is not without limitations, including limited availability, potential complications at the donor site, graft failure, and the need for additional surgical procedures, which restrict its widespread application [2]. The titanium scaffolds produced through additive manufacturing (3D printing) are widely acknowledged as a highly promising alternative to autogenous bone grafts. This is primarily due to their exceptional mechanical strength, which enables them to withstand the stress caused by mastication-related muscle activity [3]. Additionally, their intricate geometries and customizable features, achieved through layer-by-layer manufacturing, allow for tailored designs that can effectively address specific defects in individual patients [4]. However, since titanium is a bioinert material, additional biofunctionalized modifications are indispensable to facilitate adequate osseointegration in these scaffolds [5] (see Scheme 1).

Micro-scale structures have been successfully created on the initial 3D-printed titanium scaffold through the implementation of production process [6]. It is indicated that the 3D-printed titanium scaffolds, characterized by relatively rough microstructures, exhibit enhanced osseointegration compared to commercially available implants [7,8]. To further enhance its biomimetic properties, it is anticipated that a micro/nano topography, resembling the hierarchical structure of natural bone, is always developed on the surface of the titanium scaffold [9,10]. This multi-scale topography plays a crucial role in orchestrating distinct biological responses from osteoblasts [11,12]. Microstructures have been widely acknowledged for their ability to enhance cell adhesion, migration, and alignment during the initial osseointegration process. Meanwhile, nanoscale structures have been found to exert control over protein conformation, gene expression, and osteoblast

* Corresponding author. Hospital of Stomatology, Sun Yat-sen University, Guangzhou, 510055, China.
** Corresponding author. Hospital of Stomatology, Sun Yat-sen University, Guangzhou, 510055, China.
E-mail addresses: wangch373@mail.sysu.edu.cn (C. Wang), yudsh@mail.sysu.edu.cn (D. Yu).
[1] These authors contributed equally to this work.

https://doi.org/10.1016/j.mtbio.2023.100866
Received 15 August 2023; Received in revised form 15 October 2023; Accepted 11 November 2023
Available online 25 November 2023
2590-0064/© 2023 The Authors. Published by Elsevier Ltd. This is an open access article under the CC BY-NC-ND license (http://creativecommons.org/licenses/by-nc-nd/4.0/).

differentiation [13,14]. Numerous studies have demonstrated that nano/micro topography elicits superior osteogenic or angiogenic responses compared to single topography at either the nano or micro scale [15,16], a phenomenon commonly referred to as "synergistic effects" [17,18]. This occurrence can be partially attributed to the regulatory influence of nanoscale structures relying on the mechanical retention provided by the microscale structures [19]. Furthermore, the incorporation of nano-topography into scaffolds has also been found to enhance the recruitment and angiogenic activities of endothelial cells (ECs) [15,20]. Bai et al. also observed that the presence of micro/nano scale surface features had a more significant impact on angiogenesis compared to singular nano topographic cues [15]. Therefore, the integration of nanostructures onto a 3D-printed titanium scaffold that already possesses established microstructures could effectively promote both osteogenesis and angiogenesis.

Osteogenesis is a multifaceted intercellular communication process that encompasses the involvement of various cell types, including osteoblasts, osteocytes, endothelial cells (ECs), and macrophages [21,22]. Notably, the interaction between osteoblasts and ECs holds significant importance within this process [23,24]. In addition to its role in nutrient, oxygen, and waste transportation, the vasculature also plays a critical role in regulating the secretion of osteogenic signals, thereby influencing new bone regeneration [25,26]. Recent advancements have identified a distinct vascular subtype known as type H vessel, which is considered as a crucial motivator in bone regeneration through the secretion of cytokines and facilitating communication between osteogenesis and angiogenesis [27]. Relatively, osteoblasts have the ability to influence angiogenic processes through the release of paracrine factors [28,29]. Extensive evidence supports the notion that the successful formation or remodeling of bone is intricately linked to the close coordination between angiogenesis and osteogenesis [30,31]. Moreover, recent researches highlighted that implanted scaffolds were capable of modulating the interplay between angiogenesis and osteogenesis [13,32]. Hu et al. have provided evidence demonstrating that nanoscale topography can have significant effects on the development of type H vessels [33]. Liu et al. have successfully developed a novel biological membrane with abundant nano-topographic cues, and have demonstrated its ability to synergistically promote coupled osteogenesis-angiogenesis [34]. Consequently, achieving hierarchical micro/nano topographic structure with osteogenic-angiogenic coupling capacity on the surface of titanium scaffold deserves further exploration.

In recent years, the emergence of MOFs (metal-organic frameworks), a type of multifunctional nanomaterial consisting of metal ions and organic ligands, has garnered increasing attention within the academic community [35]. With advantageous characteristics such as large specific surface area, superior surface acidity and basicity, high porosity, excellent biocompatibility, and favorable biodegradability, the MOFs have been extensively explored in diverse medical fields, including but not limited to biosensing, bioimaging, drug delivery, and photodynamic therapy [36,37]. Recently, the advanced MOFs also arouse widespread concerns in the tissue engineering field [38]. The profound influence of scaffold interfacial properties on bone formation and remodeling, including topography, rigidity, charge, and hydrophilicity, has been extensively documented [39,40]. Leveraging the high structural tunability, surface modification of tailored MOFs allows for precise regulation of the interfacial properties of titanium scaffolds in terms of

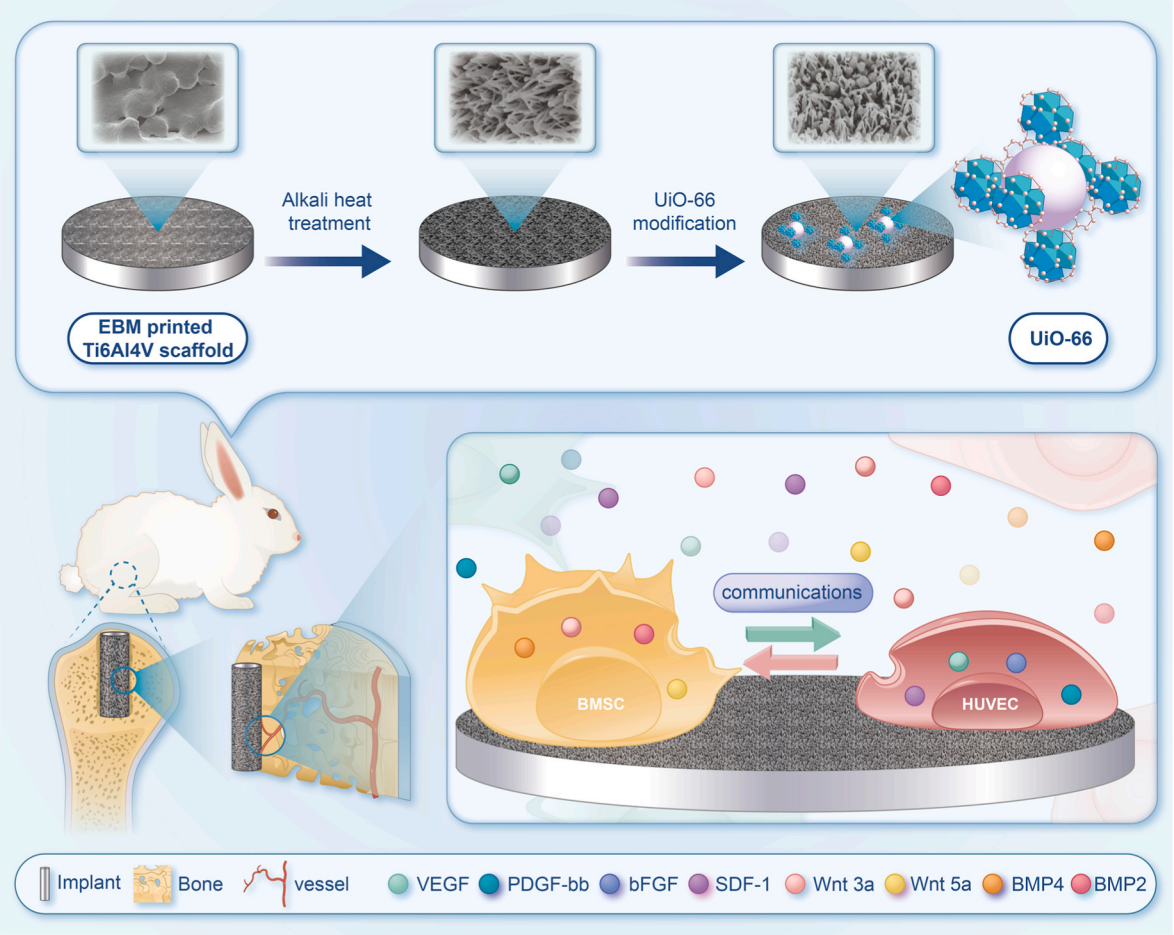

Scheme 1. A simplified illustration of manufacturing UiO-66 modified micro/nano structure on 3D printed titanium scaffold and general summary of the mechanism of the topographic structure regulating angiogenesis-osteogenesis relationship.

biomechanics, topology, and biochemistry to optimize osteogenesis performance [41]. Additionally, previous research has indicated that the incorporation of MOFs is an efficacious approach for modulating the surface topography of scaffolds [42–44].

UiO-66 is considered a prominent MOF, which is synthesized using a zirconium oxide complex [Zr_6O_4 $(OH)_4$ bridged by 1,4-benzene dicarboxylic acid ligands (H_2BDC) [45]. In addition to possessing typical advantages observed in most MOFs, such as a large specific surface area, high porosity, and the presence of catalytically active sites [46], UiO-66 distinguishes itself due to its notable attributes of low toxicity and exceptional mechanical, thermal, acidic, and aqueous stability [47,48]. The inherent stability of UiO-66 allows for more flexible incorporation of various functionalizations [49–51]. For example, depending on the high tolerance of ligand defects, the incorporation of four drugs into UiO-66 was successfully realized [52]. Consequently, the integration of UiO-66 onto the titanium scaffold provides a basis for introducing additional biological factors, such as immunomodulators and antibiotics [53,54]. Moreover, it is demonstrated that some specific types of MOFs, including UiO-66, exhibit remarkable protein absorption and retention properties [55,56], which serve as the basis for cell adhesion and cell-topography interaction [57]. While the osteogenesis promotive function of UiO-66 has been established, its potential effects on angiogenesis have yet to be determined [54]. Consequently, this study aims to investigate the impact of UiO-66 modified hierarchical micro/nano topographic structure on a 3D-printed titanium scaffold on osteogenesis, angiogenesis, and their interrelationship.

A 3D-printed titanium scaffold was produced using the techniques described in our previous research, resulting in the development of natural micro-scale formations on its surface [58]. Building upon this foundation, supplementary nanostructures modified with UiO-66 were created to establish a hierarchical micro/nano topographic structure in this study. Subsequently, the scaffold's effectiveness in the coupling of osteogenesis and angiogenesis was thoroughly examined through both in vitro and in vivo experiments.

2. Materials and methods

2.1. Materials

Ti6Al4V spherical powder of a particle size of 45–100 mm was purchased from EOS GmbH (Krailling, Germany). Terephthalic acid, zirconium oxide chloride (ZrOCl2), acetic acid, dimethylformamide (DMF), 4′,6-diamidino-2-phenylindole (DAPI), and rhodamine-phalloidin were attained from Sigma Aldrich Co. (St. Louis, USA). Dulbecco's Modified Eagle's Medium (DMEM), Minimum Essential Medium (α-MEM), penicillin-streptomycin (P/S), fetal bovine serum (FBS), bovine serum albumin (BSA) as well as fibronectin (FN) were obtained from Gibco Co. (Carlsbad, USA). RNA-Quick Purification kit was purchased from Yishan (Shanghai, China). Meanwhile, the PrimeScript RT reagent kit and SYBR Premix Ex *Taq*II kit were acquired from TaKaRa (Dalian, China). Crystal violet, cell counting kit-8 (CCK8), and LIVE/DEAD viability kit (calcein AM/PI) were supplied by Solarbio (Beijing, China). Matrigel Matrix gel was provided by Corning Inc. (Corning, USA). A vascular endothelial growth factor (VEGF) enzyme-linked immunosorbent assay (Elisa) kit was brought from Neobioscience (Shenzhen, China), while basic fibroblast growth factor (bFGF), Wnt3a and bone morphogenetic protein 2 (BMP2) Elisa kits were attained from Meimian Industrial Co. (Yancheng, China). Rabbit polyclonal antibodies against integrin β1 (ITGB1), Endomucin (EMCN), osteocalcin (OCN), mouse polyclonal antibody against CD31, fluorescein isothiocyanate (FITC)/Cyanine 3.5 (Cy 3.5)-conjugated goat anti-rabbit IgG secondary antibody and Alexa Fluor® 594 conjugated anti-mouse secondary antibody was supplied by Affinity Biosciences (Changzhou, China). Alizarin red, BCIP/NBT alkaline phosphatase (ALP) color development kit, and ALP assay kit were purchased from Beyotime Biotechnology Inc. (Shanghai, China).

2.2. Manufacture of UiO-66 modified 3D-printed titanium scaffold

The 3D-printed Ti6Al4V scaffolds were manufactured by an electron beam melted (EBM) system (ARCAM A1, Gothenburg, Sweden) in the Institute of Metal Research, Chinese Academy of Sciences. In a word, the electron beam melted the Ti6Al4V powder in a layer-by-layer manner with each layer thickness of 0.1 mm in a chamber at 550 °C and 5×10^{-4} m bar on average. After finishing, the scaffolds were cooled in a He atmosphere (200 m bar) until the temperature bed declined to 100 °C to introduce air into the chamber. Corrosive acid with ultrasonic oscillation clean was used to remove the residual powder on the microstructure. The Ti6Al4V scaffolds in the shape of a disk (10 mm × 10 mm × 2 mm) were applied in vitro experiments, while scaffolds in the shape of a cylinder (5 mm × 5 mm × 8 mm) were employed in vivo animal experiments (Fig. 1a). The titanium scaffolds were rinsed ultrasonically with distilled water, ethanol, and acetone in sequence, eventually dried before the UiO-66 loading experiment.

Alkali-heat treatment was applied for preliminary nano-topography fabrication, as mentioned previously [59]. The titanium scaffolds were immersed in a 5 M NaOH solution at 60 °C for 24 h, followed by a gentle wash in distilled water for 15 min and dried at 37 °C overnight. Subsequently, the scaffolds were heated to 600 °C at a rate of 5 °C/min in an electrical furnace. After treatment at 600 °C for an hour, the scaffolds were cooled to room temperature in the furnace.

An available and environmentally friendly hydrothermal strategy was adopted to load the UiO-66 nanocrystal onto the scaffold surface. According to the previous literature [60], $ZrOCl_2$ (187 mg), terephthalic acid (185 mg), and glacial acetic acid (1 mL) were mixed and dissolved in 20 ml of N, N-dimethylformamide (DMF). The mixture was dispersed ultrasonically for 30 min. After that, the attained solution was attenuated to concentrations of 1/2 and 1/4. The pre-treated Ti6Al4V scaffolds were put horizontally into the Teflon-lined autoclaves filled with the mixed solution and heated at 120 °C for 24 h. Then, the UiO-66 nanocrystals were obtained on the bottom of Ti6Al4V scaffolds. The Ti6Al4V scaffolds were washed three times with DMF and ethanol, then dried at 37 °C overnight. The precipitates from the mother liquor were harvested by centrifugation (5000 rpm, 5 min), rinsed with ddH_2O 3 times, and eventually dried at 37 °C overnight.

Ti6Al4V scaffolds were defined as a negatively controlled group and named TI simply. The samples treated with alkali-heat treatment were called AHT, while UiO-66 nanostructure modified AHTs were named UiO-66/AHT, 1/2UiO-66/AHT, 1/4UiO-66/AHT, corresponding to different concentration of the synthesis solutions.

2.3. Characterization

The surface topography of scaffolds was observed using a scanning electron microscope at 20 kV (SEM, Nexsa, Thermo Fisher Scientific, USA). The surface arithmetical mean height (Sa) at the micro was detected by a confocal laser scanning microscopy (CLSM, LSM700, Zeiss, Germany), while the Sa at nanoscale was examined by an atomic force microscope (AFM, Dimension Fastscan Bio, Bruker, Germany). The chemical status and crystalline structure of the synthetic nanocrystals were determined by a FTIR spectrometer (Nicolet NXR 9650, Thermo-Fisher, USA) and an X-ray diffractometer (XRD, Supernova, Japan). Software package Mercury was employed to simulate the XRD pattern of UiO-66. The surface wettability of scaffolds was ensured by measuring the contact angles of ddH2O with a contact angle goniometer (OCAH200, Dataphyscics, Germany).

For protein absorption detection, the scaffolds were immersed in α-MEM with 10 % FITC-labeled serum at 37 °C for 60 min. Then, they were observed under CLSM after PBS rinsing.

To further quantitatively assess the adsorption capability of proteins, BSA and FN were measured as targeted proteins according to Refs. [61,62]. Briefly, titanium scaffolds were incubated with the protein solution (10 mg/ml BSA or 1 mg/ml FN) at 37 °C for 2h. After then, the samples

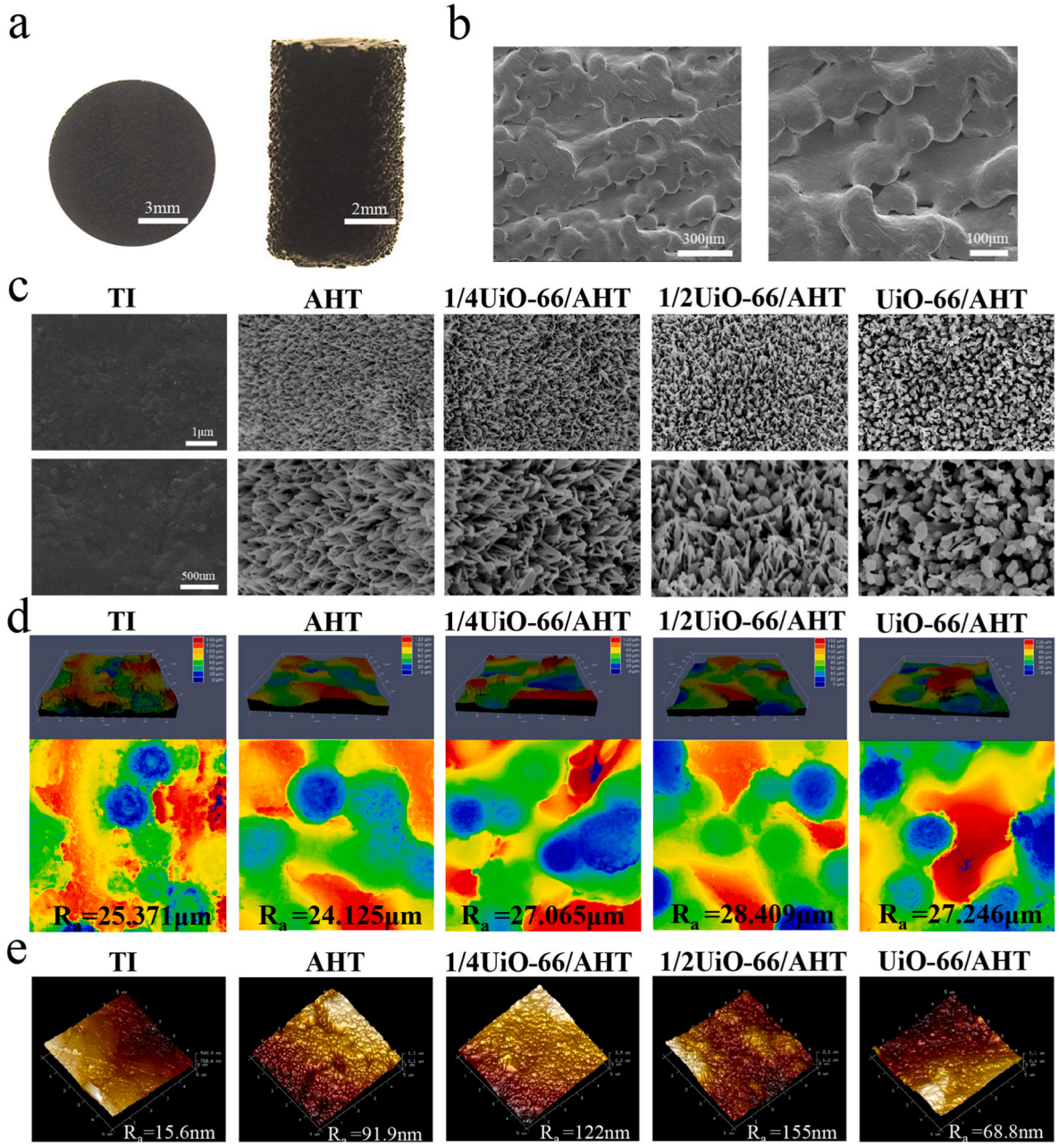

Fig. 1. Morphological observation of different scaffolds: (a) The physical images of EBM printed scaffolds; (b) Micro-topography of EBM printed scaffolds; (c) Nano-topography of TI, AHT, 1/4UiO 66/AHT, 1/2UiO-66/AHT, UiO-66/AHT; (d) Three-dimensional reconstruction view of scaffolds surface by the CLSM (at microscale); (e) Three-dimensional reconstruction view of scaffolds surface by the AFM (at nanoscale).

were taken out and washed with PBS, immersed into 5 % sodium dodecyl sulfate (SDS) solution at 37 °C under ultrasonic concussion to release the adsorbed proteins. The wash solutions were collected, and the amounts of tightly adsorbed proteins were quantified by using the BCA assay reagent kits.

2.4. Culture, adhesion, viability, and morphology of BMSCs

Human bone marrow stromal cells (BMSCs) were purchased from Procell Life Science & Technology Co. (Wuhan, China). BMSCs were cultured in α-MEM added with 10 % FBS and 1%P/S. Moreover, the culture medium was changed every 2 days. After reaching 90 % confluence, the cells were digested by 0.25 % trypsin. The incubation density of cells was 2×10^4 cells/cm^2 unless otherwise stated.

2.4.1. Cell proliferation and viability evaluation

The proliferation of BMSCs on each sample was detected with CCK-8. In brief, the cell suspension was put on each sample and cultured for 3 days, 5 days and 7 days. At the detected time points, the medium was replaced by the mixed solution at 1:9 vol ratio of CCK-8 reagent and DMEM, and then incubated at 37 °C for 1 h. After that, 100 μL solution of each sample was shifted into a 96-well plate and evaluated absorbance at 450 nm under a microplate reader (n = 3).

After incubation for 3 days, the cell viability was evaluated by a LIVE/DEAD viability kit (calcein AM/PI). Briefly, the scaffolds were rinsed by PBS for 3 times softly after the medium removal. Being diluted 1000 times with HBSS, calcein AM was placed into each well with the sample and incubated at dark for 25 min. After incubation, the scaffold was washed with PBS again and then incubated 2–3 min with PI. Subsequently, photos were captured by a CLSM (LSM780, Zeiss, Germany).

2.4.2. Adhesion observation and immunofluorescence staining

BMSCs were seeded to each group in a 24-well plate and incubated for 24 h. The cells were fixed with 4 % paraformaldehyde for 15 min, following permeabilized with PBS solution containing 1 % Triton X-100 and blocked by TBST containing 5 % BSA for 1 h. After incubation with polyclonal antibody against ITGB1 (1:200) overnight, the cells seeded in the scaffolds were incubated with Cy3.5-conjugated secondary antibody for an h, stained with phalloidin for 30min, and ultimately counterstained with Hoechst for 5 min in a dark condition. Representative images were recorded by CLSM (Olympus FV3000, Japan).

2.4.3. Cell morphology observation

BMSCs were seeded on the various Ti6Al4V scaffolds. After cultivation of 3 days, the cells were fixed with 2.5 % glutaraldehyde at 4 °C for 24 h. The scaffolds were dehydrated with graded ethanol (30, 50, 70, 90, 100 %) for 5 min in order. The cell morphology on the scaffolds was detected by SEM (Nexsa, Thermo Fisher Scientific, USA).

2.5. Osteogenesis assays of BMSCs

In osteogenesis assays, the conditional medium was firstly collected after BMSCs incubating on the scaffolds for 1 day [15]. 1 % β-glycerin, 0.05 % ascorbic acid, together with 0.01 % Dexamethasone, were supplemented into the conditional medium mentioned above to prepare an osteogenic induction medium (OM).

The expression of ALP activity and mineralized nodules in the extracellular matrix, as well as osteogenic-related genes, were investigated for evaluating the osteogenic regulatory effect of UiO-66 modified micro/nano structures. BMSCs were incubated in a 24-well plate with the OM. After cultivation for 7 days, the qualitative along with quantitative ALP activity was evaluated by BCIP/NBT ALP color development kit and ALP assay kit. After cultivation for 21 and 28 days, calcium nodules were assessed by Alizarin Red staining. In brief, the cells were rinsed with PBS twice and fixed for 30 min. After that, the cells were stained with 0.1 % Alizarin Red S for 30 min and subsequently washed with ddH_2O once. The ALP products and mineralized nodules were photographed by optical microscope.

In order to extract the total amount of RNA of BMSCs, the RNA-Quick Purification kit was adopted after cultivation with OM for 14 days. The complementary DNA was reversely transcribed from RNA by the PrimeScript RT reagent Kit. cDNA amplification and fluorescence detection were carried out by the real-time PCR system. The mRNA expression levels for each group were calculated after the difference in total cDNA amount was normalized to the GAPDH gene. The primer sequences of the osteogenesis-related genes evaluated in this research were listed in supplementary data (Fig. S1).

2.6. Culture, adhesion, viability, and morphology of HUVECs

The Human umbilical vein endothelial cells (HUVECs) were obtained from Cibioer Biosciences (Nanjing, China). HUVECs were cultivated in DMEM complemented with 10 % FBS and 1 % P/S. Other culturing conditions are the same as BMSCs. The proliferation, adhesion, viability, together with morphology of HUVECs were evaluated by the same method as aforementioned.

2.7. Angiogenesis assays of HUVECs

The effect of UiO-66 modified micro/nano structures on the migration along with the tube formation ability of HUVECs was evaluated. HUVECs were cultivated in a conditional medium collected as described in osteogenesis assays above. For migration assay, HUVECs were seeded onto a 6-well plate and cultured overnight to achieve 80–90 % confluence. Thereafter, a pipette was adopted to straightly scratch the cell monolayer. After PBS washing the non-adherent cells away, the rest of the adhesive cells were co-cultured with sample extraction for 12 h and stained with calcein AM.

For tube formation assay, the 24-well plate was pre-treated by 100 μL Matrigel Matrix and then incubated with sample extraction at 37 °C for 30 min. After the gel solidified, HUVECs at the density of 3×10^4 cells/cm^2 suspended in sample extraction were seeded on the gel. After incubating for 6 h, the vascular-like structures by HUVECs on the gel were stained by calcein AM. The results were both imaged by a fluorescence microscope (Zeiss, Germany).

To further investigate the angiogenic-related gene expression of HUVECs, the cells were incubated on the scaffolds for 3 days. In a similar manner, the gene expression level of the selected genes was assayed by RT-PCR.

2.8. Osteogenic regulation of HUVECs mediated by scaffold

2.8.1. mRNA and protein expression of osteogenic factors

Firstly, the osteogenic-related gene expression of HUVECs was detected. HUVECs were seeded to the scaffolds and cultured 3 days for mRNA extraction. After reverse transcription, RT-PCR detected the amount of related gene expression. The supernatant of the cultural medium was collected after HUVECs culturing on the scaffolds for 3 days. The secretion of related osteogenic factors (BMP-2, Wnt3a) was assessed by the corresponding Elisa Kit.

2.8.2. Osteogenic regulation of HUVECs

In order to survey the migration and osteogenic activity of BMSCs adjusted by HUVECs mediated by different scaffolds, a co-culture transwell system was adopted.

In the migration assay, HUVECs (5×10^4 cells/well) were incubated on the scaffold in the 24-well plate for 48 h. Afterward, BMSCs (4×10^4 cells/well) were seeded onto the upper chamber (pore size = 8 μm) while the complete medium was refreshed in the lower chamber. After co-culturing for 24 h, the transmembrane BMSCs were fixed with 4 % paraformaldehyde for 30 min and then stained with 0.4 % crystal violet for 20 min. The optical microscope was employed to photograph the migrated BMSCs at 5 random spots. The representative optical images of migrated BMSCs from different groups were recorded at 5 random spots. The number of migrated cells was calculated by ImageJ.

In the osteogenic differentiation assay, HUVECs (2×10^4 cells/well) were seeded on the scaffold in the lower chamber. After incubation of 48 h, BMSCs (1×10^4 cells/well) were seeded on the upper chamber of the transwell system (pore size = 0.4 μm) and co-culture for 7 days. The cultural medium was replaced with an osteogenic medium after achieving 80 % confluence and continued to refresh every 2 days. Eventually, qualitative and quantitative ALP activity was evaluated in the upper chamber, as mentioned above.

2.9. Angiogenic regulation of BMSCs mediated by scaffold

2.9.1. mRNA and protein expression of angiogenic factors

To evaluate the angiogenic promotive effect of BMSCs inspired by scaffolds, mRNA expression of angiogenic factors was detected by RT-PCR. Cell cultivation, mRNA extraction, reverse transcription, and RT-PCR proceeded as described before. Elisa kit was employed to detect the secretion amount of angiogenic factors (VEGF, bFGF).

2.9.2. Angiogenic regulation of BMSCs

The co-culture transwell system was also utilized to evaluate the migration and tube formation capacity of HUVECs. BMSCs were seeded onto the scaffold in the 24-well plate and incubated for 48 h. The cultural medium was refreshed, and HUVECs (2×10^4 cells/well) were seeded in the upper chamber.

After two types of cells were co-cultivated in that transwell system for 24 h, the migrated HUVECs through the porous membrane (pore size = 8 μm) were investigated. In tube formation assay, the HUVECs were seeded on the upper chamber with 30 μL Matrigel Matrix gel and co-

cultivated with BMSCs for 6 h. Crystal violet was adopted to stain the migrative cells and tubular structures the same as mentioned above.

2.10. Animals and surgical procedures

2.10.1. Implantation surgery

The entire process of the animal experiment was performed under the approval of the Experimental Animal Ethics Committee of Sun Yat-sen University and conformed to the relevant laws and institutional guidelines. The ethical approval number provided by the Ethics Committee is SYSU-IACUC-2022-002000. Fifteen adult male New Zealand white rabbits (2.5–3.0 kg per rabbit) were used for this implantation surgery experiment. The rabbits were divided into three groups randomly to evaluate the osteogenesis and angiogenesis in vivo. Briefly, the rabbits were intravascular anesthetized. With fur at the femur shaved and disinfected, a cylindrical defect was made with a surgical electrical drill under cooled sterile saline irrigation. A scaffold was inserted softly into the hole, and the wound was sutured.

Six weeks after implantation surgery, the rabbits were sacrificed for the assessment of bone tissue regeneration and vascularization. The scaffolds and the surrounding femurs were harvested and fixed in 10 % paraformaldehyde for the following experiments.

2.10.2. Histological analysis

The femoral tissue around the scaffolds was first decalcified in 10 % (w/v) EDTA solution (pH = 7.4) for 28 days. After decalcification, the femoral tissue was dehydrated in an increasing series of ethanol and then embedded in paraffin wax blocks. The hard bone tissue slices were cut to vertical cross-sections with 5 μm thickness and stained with HE or Goldner's trichrome to observe histological features of tissue around the scaffold under the optical microscope (Olympus, Japan).

For coupling osteogenesis-angiogenesis relationship observation, the sections were adopted immunohistochemical staining with OCN or CD31. To survey type H vessel distribution, the sections were immunofluorescence stained with EMCN, CD31, and DAPI in immunohistochemical staining assay, and the sections were incubated with citrate buffer(pH = 6.5)at 80 °C to perform the antigen retrieval first. Afterward, the sections were incubated with anti-CD31 or anti-OCN antibody at 4 °C overnight, followed by further incubating with horseradish peroxidase (HRP) labeled goat anti-mouse/rabbit secondary antibody for another 30 min. At last, the sections were dealt with 3,30-diaminobenzidine tetrahydrochloride (DAB) and counterstained with hematoxylin. In the immunofluorescence staining assay, the sections were permeabilized with 0.3 % Triton X-100 at room temperature for 10 min and blocked with TBST containing 5 % BSA for 30 min. After that, the sections were incubated with anti-EMCN and anti-CD31 antibodies at 4 °C overnight and then counterstained with FITC-conjugated goat anti-rabbit IgG secondary antibody and Alexa Fluor® 594 conjugated anti-mouse secondary antibody for an hour, eventually stained with DAPI for 5 min. The sections with immunohistochemical staining were observed by optical microscope, and those with immunofluorescence staining were observed under CLSM.

2.11. Statistical analysis

All data are presented as means ± standard deviation. One-way ANOVA or unpaired *t*-test was employed to analyze the statistical difference among groups with the software package GraphPad Prism 8.0 (GraphPad Software Inc., San Diego, USA). Moreover, when $p < 0.05$, the difference was regarded as statistically significant.

3. Results and discussion

3.1. Surface characterization

The EBM-printed titanium scaffold on naked eye observation was shown in Fig. 1a. Due to the layer-by-layer productive technology, natural microstructure formed on the surface of EBM-printed titanium scaffold. As shown in Fig. 1b, circular microstructures with a diameter of 50 μm–70μm on the EBM-printed titanium scaffold surface exhibited a continuous valley-peak pattern, which was consistent with a previous study [63]. The surface topography and roughness of TI, AHT, 1/4UiO-66/AHT, 1/2UiO-66/AHT, and UiO-66/AHT were characterized by SEM, CLSM, and AFM. The nanostructures of each group were displayed in Fig. 1c. SEM images at high magnification revealed that the surface of the TI group looked smooth at nanoscale, while the scaffolds treated with alkali-heat were full of ordered linear nanorods with approximately 300–350 nm in length. Besides, numerous mesopores with 100–150 nm in length formed between adjacent clusters of nanorods. In UiO-66 modification groups, hexagon nanocrystals with a size of 80–120 nm were covered on the nanorods or mesopores randomly, and the numbers of crystals increased from 1/4UiO-66/AHT to UiO-66/AHT.

To further evaluate the topographic change at different scales, the 3D view of each scaffold was reconstructed by the CLSM (Fig. 1d) and AFM (Fig. 1e). The images of CLSM indicated that the microroughness of scaffolds fluctuated from a low of 24 μm–28.5 μm, agreeing with the report that raw 3D-printed scaffolds possess high rough surfaces with R_a about 25 μm [63]. The results revealed that nanostructures had weak impaction on the original topography and roughness at the microscale. In addition, the ordered nanorods in AHT improved the nanoroughness of scaffolds from 15.6 nm to 91.9 nm, while the random cover of UiO-66 crystals further elevated the nanoroughness in 1/4UiO-66/AHT and 1/2UiO-66 AHT. However, the nanoroughness in UiO-66/AHT decreased oppositely, which could be explained by the fact that most prominent nanorods were covered by two-dimensional nanosheets. Considering the results above, the micro/nano topography was successfully constructed.

To determine the crystalline structure and chemical status of the nanocrystals on the scaffold surface, precipitates in the mother solution were measured by XRD and FTIR spectroscopy. As shown in Fig. 2a, absorption bands at 680 cm^{-1} and at 1510 cm^{-1} were observed due to stretching vibrations in the Zr–O bond and C═C bond in benzene ring [48]. Moreover, the peaks at 1395 cm^{-1} and 1590 cm^{-1}, respectively, reflected the symmetrical and unsymmetrical stretching vibrations in the C═C–O bond of H_2BDC. The peak positions and their assignment of FTIR conformed to the former references about UiO-66 synthesis [64]. XRD patterns (Fig. 2b) of UiO-66 coating groups and the one simulated in software all demonstrated the characteristic peaks at $2\theta = 7.3°$, 8.5°, consistent with previously reported literature [65]. The results of FTIR and XRD implied that the pure UiO-66 crystals were successfully composed and loaded on the surface of scaffolds.

The surface wettability of scaffolds was displayed in Fig. 2c. The contact angle of the TI scaffold was beyond 80°, whereas that for AHT was less than 10°. Furthermore, the contact angle gradually increased from 1/4UiO-66/AHT to UiO-66/AHT from 38° to 60° with the ascending trend of UiO-66 nanocrystals, in agreement with former literature [66]. The hydrophilicity of the scaffold was influenced by its chemical composition and surface roughness [67]. The enhanced hydrophilicity observed in the AHT could be attributed to the presence of numerous hydroxyl groups [68,69]. Consequently, the UiO-66 modification groups displayed an increasing hydrophobic trend with the higher loading quantity. The introduction of hydroxyl through alkali-heat pretreatment effectively enhanced the complexation between the UiO-66 coating and the titanium surface. Besides electrostatic adsorption, the functional groups and metal ions of MOFs form chemical covalent bonds (such as esterification) and intermolecular hydrogen bonds with the hydroxyl groups [70–72].

As shown in Fig. 2d and e, scaffolds with nanostructures all displayed higher serum protein adsorption properties than the TI group ($p < 0.05$). Additionally, the enhancement of serum protein absorption capability was observed through further modification of UiO-66 with increasing dose. BSA mimics total protein in human plasma, while FN is the most

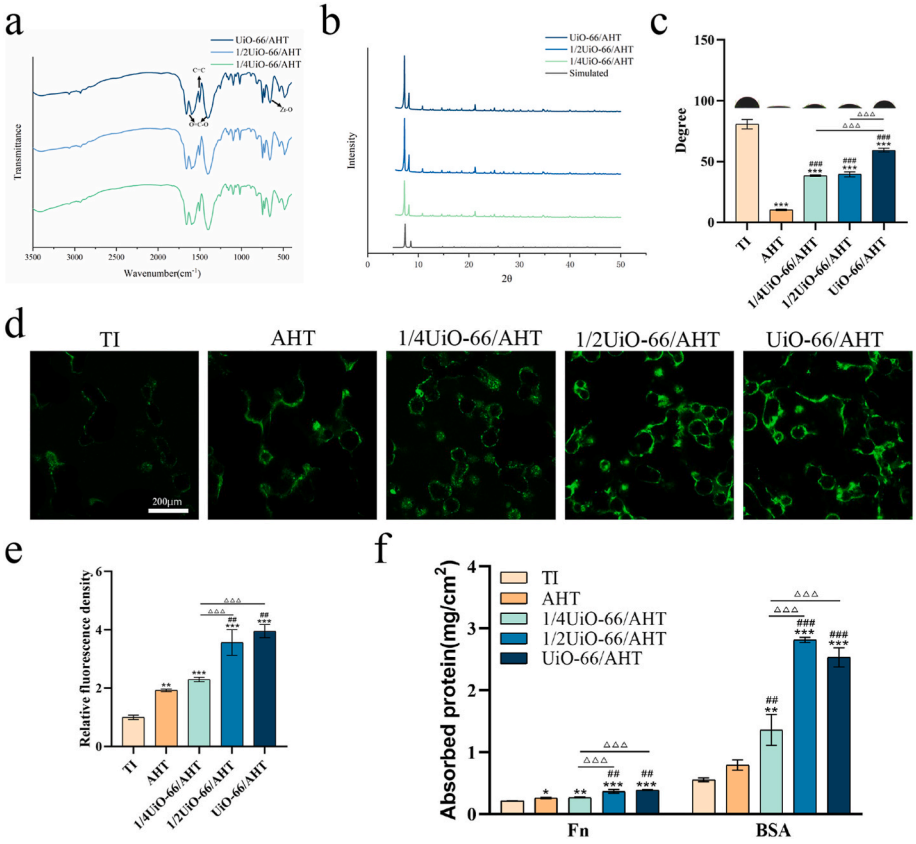

Fig. 2. Surface characteristics of different scaffolds: (a) FTIR spectra of synthetic UiO-66 nanocrystals; (b) XRD patterns of the simulated and synthetic UiO-66 nanocrystals; (c) Qualitative results of contact angle; (d) Fluorescent images of serum protein absorption on scaffolds; (e) Quantitative analysis of fluorescence density; (f) Quantitative analysis of absorbed BSA and FN on scaffolds; $^{*}p < 0.05$,$^{**}p < 0.01$, $^{***}p < 0.005$ compared to TI group; $^{\#\#}p < 0.01$, $^{\#\#\#}p < 0.005$ compared to AHT group; $^{\triangle\triangle\triangle}p < 0.005$.

absorbed adhesive protein among the thousands of proteins present in human plasma [73]. The quantitative assessment in Fig. 2f further revealed that the protein adsorbing ability of TI was relatively lowest when 1/2UiO-66/AHT and UiO-66/AHT absorbed most protein, either for BSA or for FN ($p < 0.05$).

The adsorption of proteins is influenced by various surface physicochemical properties, including surface wettability, roughness, topography, charge, and chemistry [55]. While a hydrophobic surface promotes protein absorption, it may also cause denaturation of the absorbed proteins [57]. Therefore, it is crucial to regulate surface wettability within an appropriate range to facilitate increased protein absorption while preserving its native conformation. Several studies have also demonstrated that the moderate surface wettability, characterized by water contact angles of 40–50°, is indicative of hydrophilicity satisfaction [74,75]. The hydrophilicity of the titanium surface can be effectively regulated within an optimal range by employing a combination of alkali-heat treatment and the incorporation of hydrophobic UiO-66. Besides hydrophobicity, nanoroughness has been found to enhance protein absorption by increasing surface free energy and altering the adsorption mechanisms from protein monolayer to multilayer adsorption [57,76]. It is the topography, rather than roughness or wettability, that primarily determines the protein adsorption ability, as proteins tend to aggregate within the physical nano-traps formed by the convex and concave features of nanostructures [57,77]. Therefore, the mesopore created by AHT effectively improved protein absorption. Additionally, recent research has demonstrated that certain types of MOFs, such as UiO-66, possess remarkable protein adsorption and retention properties due to their large specific surface areas and pore volumes [55,56]. This is significant as protein adsorption serves as the primary stage in the implantation of scaffolds within living organisms and is crucial for subsequent biological processes [78]. Extensive research has consistently demonstrated that scaffolds exhibiting a high affinity for protein adsorption can induce the activation of integrin expression, leading to enhanced cell adhesion, spreading, and ultimately facilitating successful osseointegration [79,80]. For example, Griffin et al. conducted a study that implants with better protein absorption ability after argon plasma treatment performed better osteogenic as well as angiogenic activity [81]. Fu et al. provided evidence for the positive impact of nano-topography on protein absorption, as well as the promotion of angiogenic and osteogenic activity [82]. Wu et al. developed a novel nanocoated scaffold that exhibited high protein absorption and confirmed its capability to promote osteogenesis and angiogenesis [83].

3.2. *Viability, proliferation adhesion, and morphology of BMSCs on scaffolds*

Live/dead staining assay and CCK-8 assay were applied to appraise the viability and proliferation of BMSCs on the scaffold with time passing by (Fig. 3a–c). Live/dead staining assay results revealed that most BMSCs of all groups were still alive, and simultaneously, only several dead cells existed. More live cells were observed on 1/2UiO-66/AHT than the TI and AHT group ($p < 0.05$). The results of CCK8 revealed that the cell proliferation elevated in a time-dependent manner from day 3 to day 7. As time went to day 7, the 1/2UiO-66/AHT turned out to be the group with the highest cell proliferation ($p < 0.01$), while cells on UiO-66/AHT displayed less proliferative activities than AHT ($p < 0.01$). According to reports, the utilization of nanoMOFs at low or appropriate concentrations has been found to enhance cell proliferation and viability, whereas high concentrations have been observed to inhibit these processes [42,84]. Furthermore, the findings of this study suggest

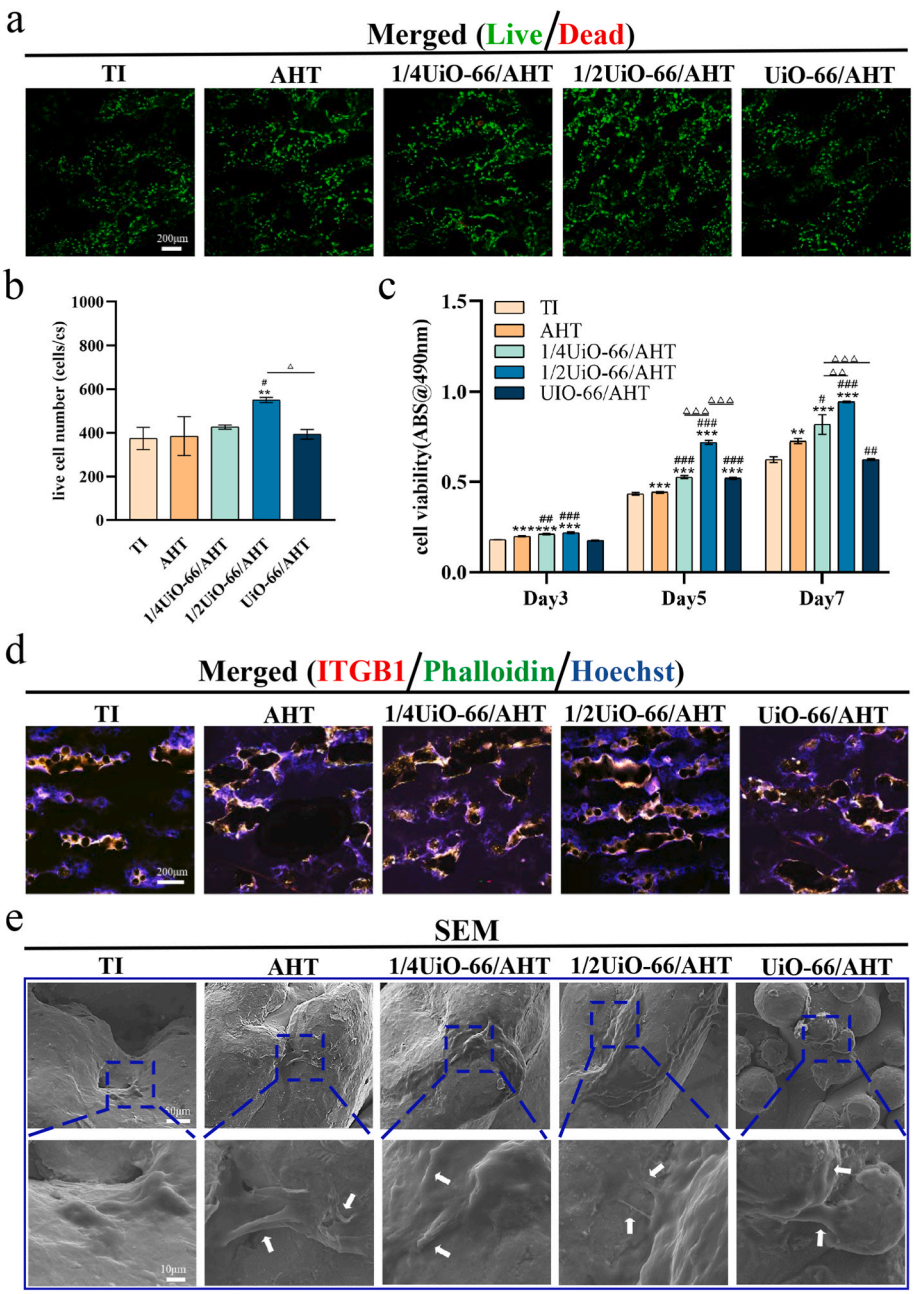

Fig. 3. Adhesion, morphology, viability, and proliferation of BMSCs on different titanium scaffolds: (a) Representative images of live/dead staining; (b) Quantitative counting of live cells on scaffolds; (c) Cell proliferative results examined with CCK-8 assays after 3, 5, and 7 days of seeding; (d) Representative immunofluorescence staining of ITGB1, Phalloidin, and DAPI; (e) SEM morphology of BMSCs incubated on the scaffolds for 3 days (white arrows, polygonal lamellipodium protrusions); $^{**}p < 0.01$, $^{***}p < 0.005$ compared to TI group; $^{\#}p < 0.05$, $^{\#\#}p < 0.01$, $^{\#\#\#}p < 0.005$ compared to AHT group; $^{\triangle}p < 0.05$, $^{\triangle\triangle}p < 0.01$, $^{\triangle\triangle\triangle}p < 0.005$.

that despite UiO-66's high biocompatibility resulting from its exceptional stability [48], excessive loading of this material can still induce cytotoxic effects during the later stages of cultivation.

The initial adhesion of BMSCs was investigated by immunofluorescence staining. As shown in Fig. 3d, the cells in all groups were inclined to accumulate in the concave of the EBM-printed titanium scaffolds. TI scaffolds displayed the least adherent cells, while 1/2UiO-66/AHT scaffolds adhered to the most. Additionally, it was observed that 1/2UiO-66/AHT exhibited the highest level of integrin expression, a crucial cell surface receptor involved in cell adhesion [85] (Fig. S2). Similarly, The SEM images at low magnification also revealed that most adherent cells existed in 1/2UiO-66/AHT among 5 groups (Fig. 3e). The immunofluorescence staining and SEM images provided confirmation that the micro/nano topographic structure of the scaffolds facilitated cell attachment [19]. Moreover, the SEM images at higher magnification revealed that the bone marrow-derived mesenchymal stem cells (BMSCs) in the tissue engineering (TI) groups exhibited a short spindle shape, while those in the groups with nanostructures displayed more extensive cell spreading and active polygonal lamellipodium extensions. The findings of this study align with previous research indicating that nanostructures promote cell spreading and extensions by facilitating binding between transmembrane integrin and peptide ligands derived from absorbed proteins [15,17]. More importantly, the BMSCs exhibited improving spread, adhesion, and displayed a greater propensity for osteogenic differentiation [86].

3.3. Osteogenic differentiation of BMSCs on scaffolds

ALP is commonly employed as a marker for evaluating osteogenesis [54]. Qualitative analysis of ALP staining revealed that the UiO-66/AHT groups exhibited higher levels of ALP production compared to the AHT and TI groups (Fig. 4a). The quantitative result further evidenced that 1/2UiO-66/AHT group secreted the highest amount of ALP product (Fig. 4c). The result of ECM mineralization by Alizarin staining was shown in Fig. 4b and d, cells on the 1/4UiO-66/AHT and 1/2UiO-66/AHT possessed significantly higher ECM mineralized activity than that on TI and AHT ($p < 0.05$). Among the three UiO-66 groups, though the 1/2UiO-66/AHT group showed the highest ECM mineralization level, there is no significant difference between them at day 21. Moreover, the 1/2UiO-66/AHT turned to display the best ECM mineralization at day 28 ($p < 0.05$). In order to further assess the osteogenic activity of cells on different scaffolds at the molecular level, the mRNA expression levels of osteoblast-related markers were investigated by RT-PCR (Fig. 4f). The results showed that cells on 1/4UiO-66/AHT and 1/2UiO-66/AHT displayed superior expression of ALP, RUNx2, and OPN than other groups ($p < 0.05$). Meanwhile, 1/2UiO-66/AHT exhibited the markedly highest expression of OCN ($p < 0.005$). In brief, UiO-66 hybrid micro/nano topographic structures on the 1/2UiO-66/AHT group resulted in the optimal promotion of osteogenic differentiation.

Cells do not interact directly with the topographic cues but sense it through peptide ligands derived from absorbed proteins to transmembrane receptors, such as integrin [17]. The integrin-ligand binding leads to the formation of intracellular focal adhesion complexes [(e.g., focal adhesion kinase(FAK)] and subsequent up-regulation of FAK/-MAPK and ILK/β-catenin signaling pathways [87,88]. In the described process above, the extracellular physical cues are transferred to intracellular biochemical signals, a process known as indirect mechanotransduction [89]. The topographic structures on the titanium scaffold surface could regulate the expression of integrin subunits to further regulate cell behavior by altering the amount, type, and configuration of the adsorptive proteins [40]. Furthermore, the binding of integrin-mediated by surface topography can lead to the reorganization

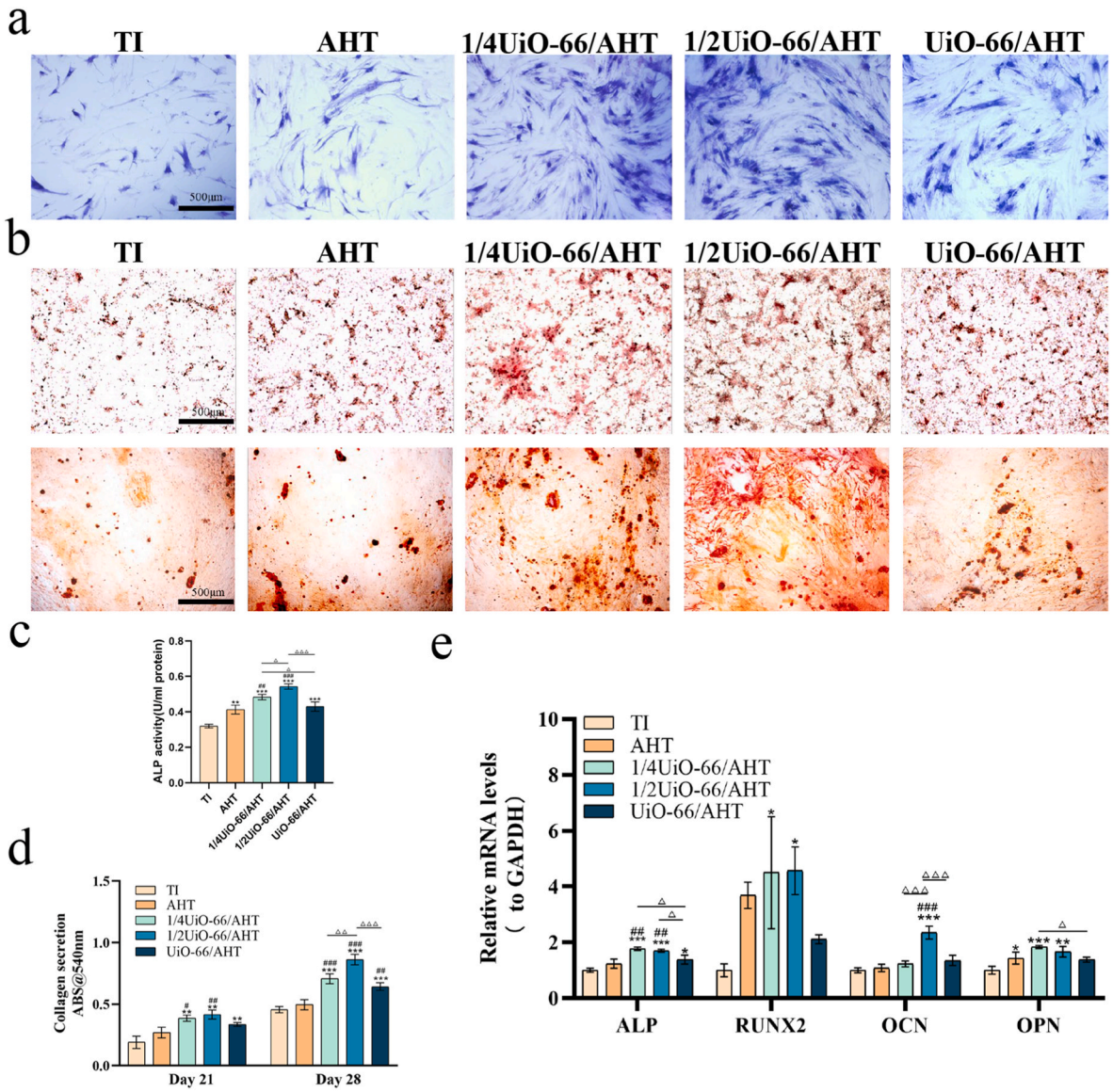

Fig. 4. In vitro osteogenic differentiation of BMSCs incubated on different scaffolds: (a) Representative images of ALP staining results of BMSCs; (b) Representative results of mineralized nodules at Day 21 and Day 28; (c) Quantitative analysis of ALP activity; (d) Semi-quantitative analysis of Alizarin Red staining of BMSCs at Day 21 and Day 28; (e) Relative osteogenic-related mRNA expression of BMSCs; $^{*}p < 0.05$, $^{**}p < 0.01$, $^{***}p < 0.005$ compared to TI group, $^{\#}p < 0.05$, $^{\#\#}p < 0.01$, $^{\#\#\#}p < 0.005$ compared to AHT group, $^{\triangle}p < 0.05$, $^{\triangle\triangle}p < 0.01$, $^{\triangle\triangle\triangle}p < 0.005$. (For interpretation of the references to colour in this figure legend, the reader is referred to the Web version of this article.)

of the cytoskeleton, subsequently affecting the shape of the nucleus and potentially the orientation of chromosomes, a phenomenon known as direct mechanotransduction [89]. Additionally, the introduction of UiO-66 as an additional modification to the nano-topography resulted in enhanced absorption of serum proteins [55]. Superior expression of integrin β1 and reorganization of the cytoskeleton were both observed in 1/2UiO-66/AHT. Consequently, 1/2UiO-66/AHT, with its heightened protein adsorption capacities, positively influenced the interaction between cells and topography, thereby promoting cell adhesion, proliferation, and differentiation through direct or indirect mechanotransduction mechanisms.

The hierarchical micro/nano topography has the potential to enhance the osteogenic promoting effect by replicating the microscale collagen fiber structure and nanoscale hydroxyapatite composition of natural bone [90,91]. This finding aligns with the observation that both the AHT and UiO-66/AHT groups exhibited elevated levels of osteogenic markers. Several investigations on scaffold topography have focused on emulating the nanoscale topography of natural bone, which comprises hydroxyapatite nanocrystals ranging from 2 to 5 nm in thickness and 20–80 nm in length [40,92,93]. Dably et al. found that comparing nanostructures aligned in totally ordered or random pattern, cells in moderate disorder mode performed higher potential of osteogenic differentiation [94]. Other researches also demonstrated that nanopatterns characterized by precise order resulted in reduced cell adhesion [95,96]. Therefore, the incorporation of rod/crystal hybrid nanostructures on 1/2UiO-66/AHT reasonably increased the degree of disorder in nano topographic patterns, thereby yielding the most favorable outcome for osteogenic differentiation.

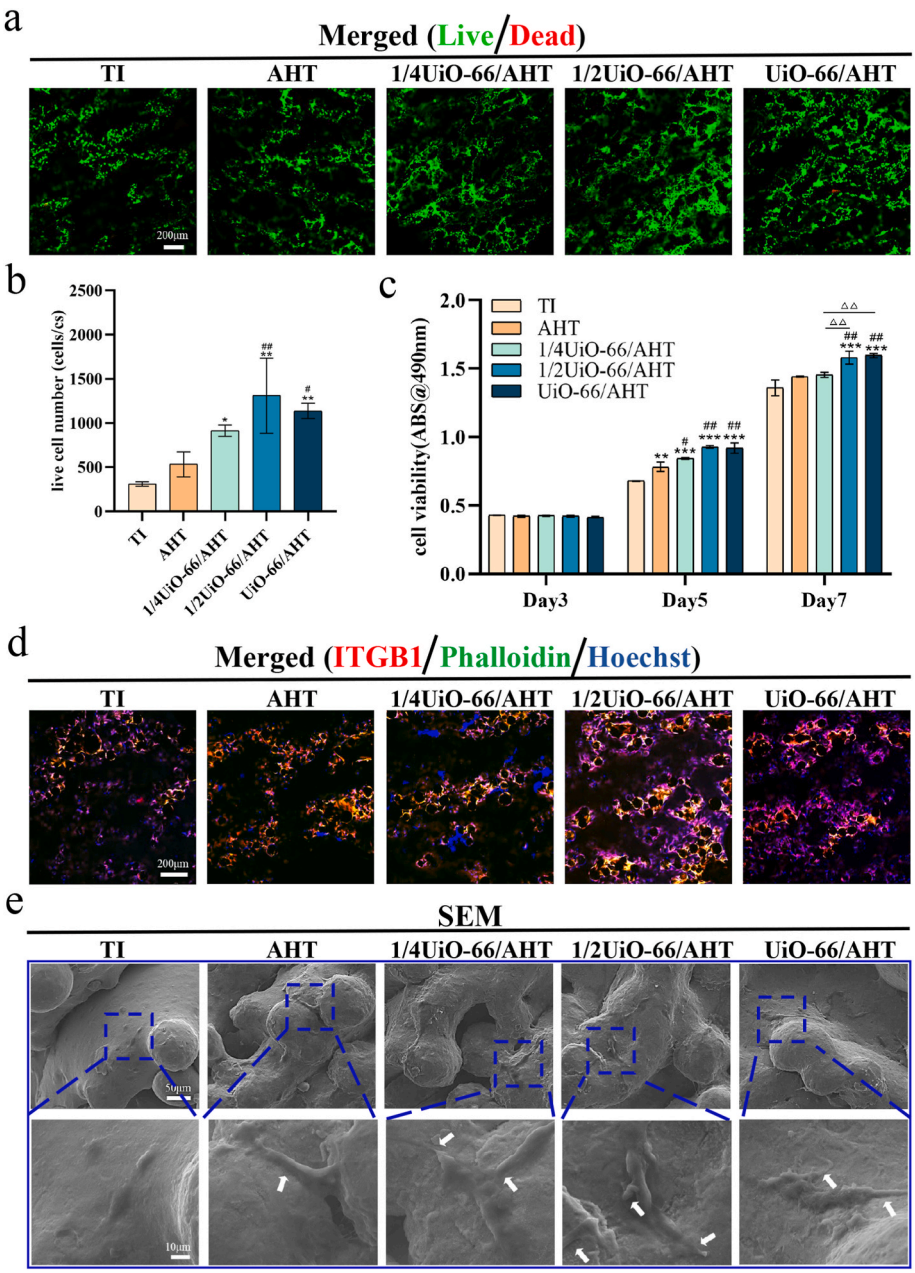

Fig. 5. Adhesion, morphology, viability, and proliferation of HUVECs on different scaffolds: (a) Representative images of live/dead staining; (b) Quantitative caculation of live cells on scaffolds; (c) Cell proliferative results examined with CCK-8 assays after 3, 5, and 7 days of seeding; (d) Representative immunofluorescence staining of ITGB1, Phalloidin, and DAPI; (e) SEM morphology of HUVECs cultured on the scaffolds for 3 days (white arrows, polygonal lamellipodium protrusions); $^{*}p < 0.05$, $^{**}p < 0.01$, $^{***}p < 0.005$ compared to TI group, $^{\#}p < 0.05$, $^{\#\#}p < 0.01$ compared to AHT group, $^{\triangle\triangle}p < 0.01$.

3.4. Adhesion, morphology, viability, and proliferation of HUVECs on scaffolds

In views of the live/dead cells assay, nearly all adhesive cells on scaffolds were alive (Fig. 5a). The quantitative counting result in Fig. 6b displayed that more alive cells attached on the 1/2UiO-66/AHT and UiO-66/AHT than that on AHT and TI ($p < 0.05$). The results of the CCK8 assay displayed that the cells in different groups had similar metabolic activities on day 3 (Fig. 5c). During the late cultivation period, the findings exhibited a comparable trend to the live/dead cells assay, indicating that 1/2UiO-66/AHT and UiO-66/AHT groups demonstrated superior proliferation compared to other groups ($p < 0.05$). In contrast to BMSC, HUVECs exhibited greater tolerance towards high doses of UiO-66.

The initial adhesion images revealed that all scaffolds facilitated HUVEC adhesion, with 1/2UiO-66/AHT exhibiting the most favorable adhesion property (Fig. 5d). Similar to the results observed in BMSCs, the enhanced protein adsorption property induced by UiO-66 modified nanostructures enhanced the adhesion of HUVECs. The surface topography and composition had a profound influence on the morphology and orientation of endothelial cells [97]. In this study, the cells in the TI group looked round and arranged individually, whereas cells on scaffolds with nanostructures displayed elongated spindles with numerous extensive filopodia, interconnected in a net-like pattern (Fig. 5e). Filopodia, a distinguishing feature of a specialized subtype of endothelial cells known as tip cells, are primarily found at the leading edge of branching blood vessels during the process of neo-angiogenesis [98]. These tip cells play a crucial role in guiding the directional growth of sprouts [99]. The formation of filopodia depends on integrin-mediated adhesion to the local extracellular matrix [100]. Therefore, combining the result of immunohistochemical staining, the nano-topographic structure may upregulate the activation of tip cells due to the enhancement of integrin expression and adhesion.

3.5. Angiogenic differentiation of HUVECs on scaffolds

The migration of endothelial cells serves as the primary stage in the development of new blood vessels [101]. The nanostructures on AHT and UiO-66/AHT groups, particularly in the 1/2UiO-66/AHT group, significantly enhance the migratory capability of HUVECs, as demonstrated by the wound healing assay (Fig. 6a–b). The enhanced migratory action may be attributed to the enhanced viability of HUVECs achieved through modification of UiO-66 nanostructures [15]. Additionally, the adhesion mediated by integrin is fundamental of cell migration [102]. The improved cell adhesion on 1/2UiO-66/AHT also facilitated cellular movement. The formation of tube-like structures by ECs is a critical step

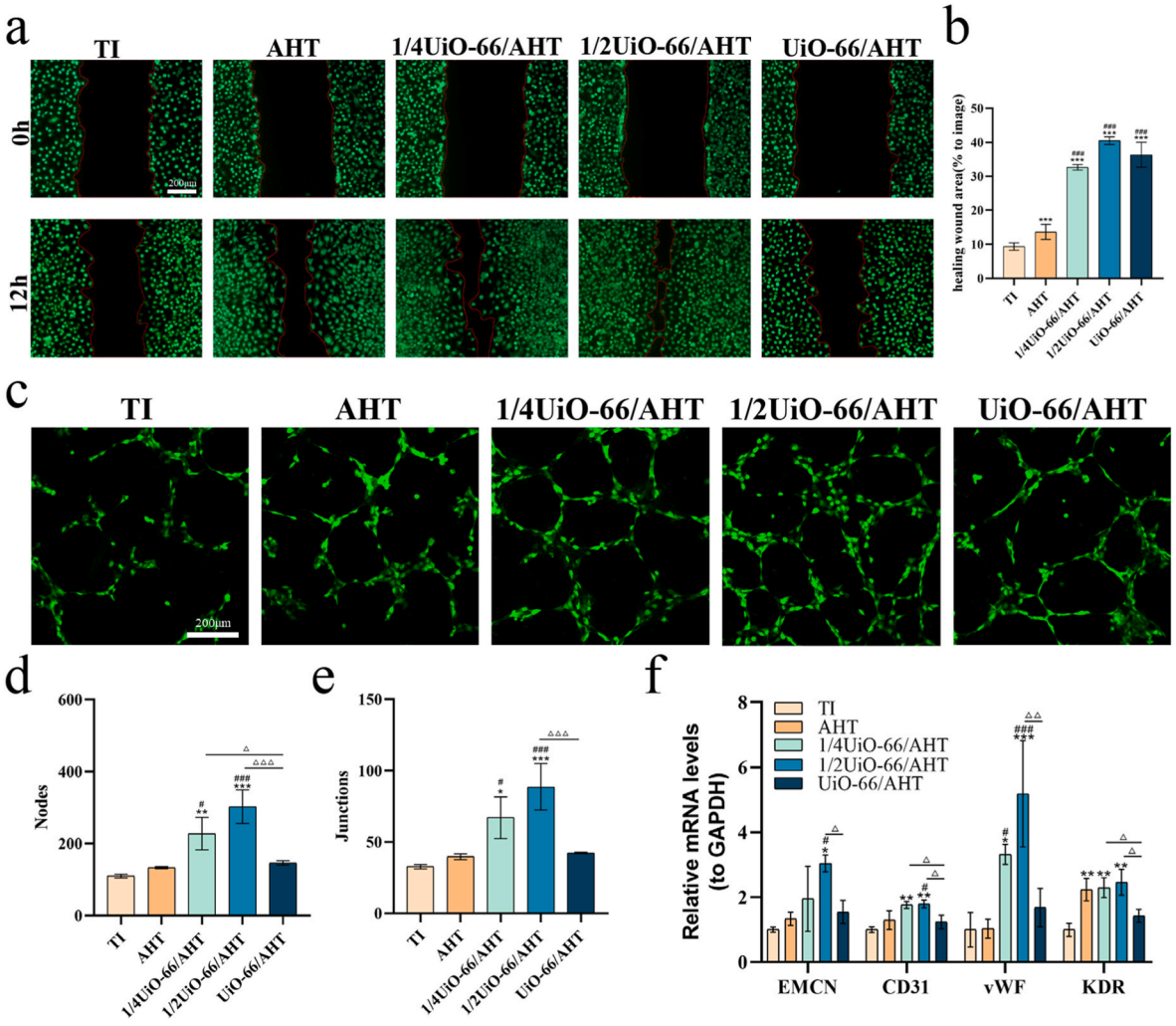

Fig. 6. In vitro angiogenic differentiation of HUVECs cultured on different scaffolds: (a) Representative wound healing migration images; (b) Quantitative analysis for the migrated HUVECs in scratch wound healing assay (0 h, 12 h); (c) Representative fluorescence images of tube formation; (d) Quantitative analysis of nodes and (e) junctions of tubular structures; (f) Relative angiogenic-related mRNA expression of HUVECs; $^{*}p < 0.05$, $^{**}p < 0.01$, $^{***}p < 0.005$ compared to TI group, $^{\#}p < 0.05$, $^{\#\#}p < 0.01$, $^{\#\#\#}p < 0.005$ compared to AHT group, $^{\triangle}p < 0.05$, $^{\triangle\triangle\triangle}p < 0.005$.

in angiogenesis [101]. The results of the tube-like structure formation assay revealed that tube networks were better connected on 1/4/UiO-66/AHT and 1/2/UiO-66/AHT, indicating that the modification of UiO-66 nanocrystals with a medium concentration had a significant impact on angiogenesis (Fig. 6c–e). Bai et al. found that nano-topography, particularly micro/nano topography, had the potential to stimulate greater nitric oxide (NO) synthesis compared to a smooth titanium surface, thereby enhancing the tube formation activity of ECs [15]. Besides, Tang et al. reported a novel silk fibroin film with microstructure could promote angiogenesis via upregulating the

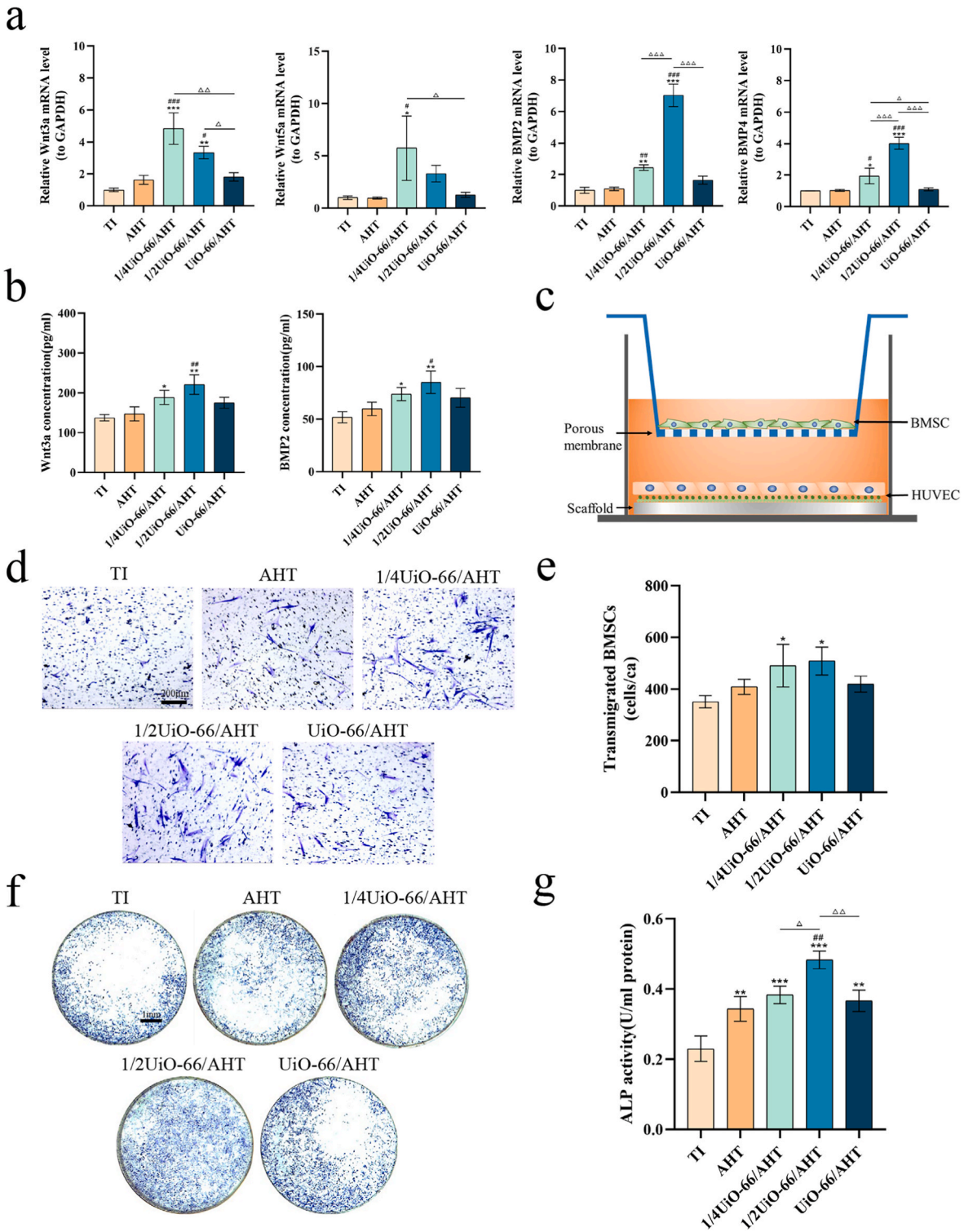

Fig. 7. In vitro osteogenic regulation of HUVECs on different scaffolds: (a) Relative osteogenesis-related mRNA expression of HUVECs; (b) Quantified analysis of BMP2 and BMP4 concentrations secreted by HUVECs in Elisa kit; (c) Schematic illustration of Scheme of BMSCs and HUVECs co-culture system; (d) Representative images of transmigrated BMSCs in co-culture system; (e) Quantitative analysis for transmigrated BMSCs; (f) Representative images of ALP staining in co-culture systems; (g) Quantitative analysis for ALP activity; $^{*}p < 0.05$, $^{**}p < 0.01$, $^{***}p < 0.005$ compared with TI group, $^{\#}p < 0.05$, $^{\#\#}p < 0.01$, $^{\#\#\#}p < 0.005$ compared with AHT group, $^{\triangle}p < 0.05$, $^{\triangle\triangle}p < 0.01$, $^{\triangle\triangle\triangle}p < 0.005$.

expression of bFGF and VEGF [103]. Consequently, the distinctive nanostructures, particularly those present on 1/2UiO-66/AHT, may also induce the autocrine release of angiogenic factors, thereby further enhancing the functional capabilities of ECs.

The detected results of mRNA expression about angiogenesis-related genes illustrated that the expression of vWF, CD31, and KDR was upregulated in 1/4/UiO-66/AHT and 1/2/UiO-66/AHT (Fig. 6f). It is evidenced that increased expression of vWF and CD31 facilitate the migration and angiogenesis progression [15]. The high expression of KDR indicated that ECs were in a highly proliferative condition [31]. In addition, EMCN expressed highest in 1/2UiO-66/AHT ($p < 0.05$), which is also highly expressed in Type H blood vessels, the hallmark of coupling osteogenesis-angiogenesis relationship [30]. Briefly, UiO-66/AHTs, especially 1/2UiO-66/AHT, significantly facilitated the adhesion, viability, morphology, and functionality of ECs to promote angiogenesis.

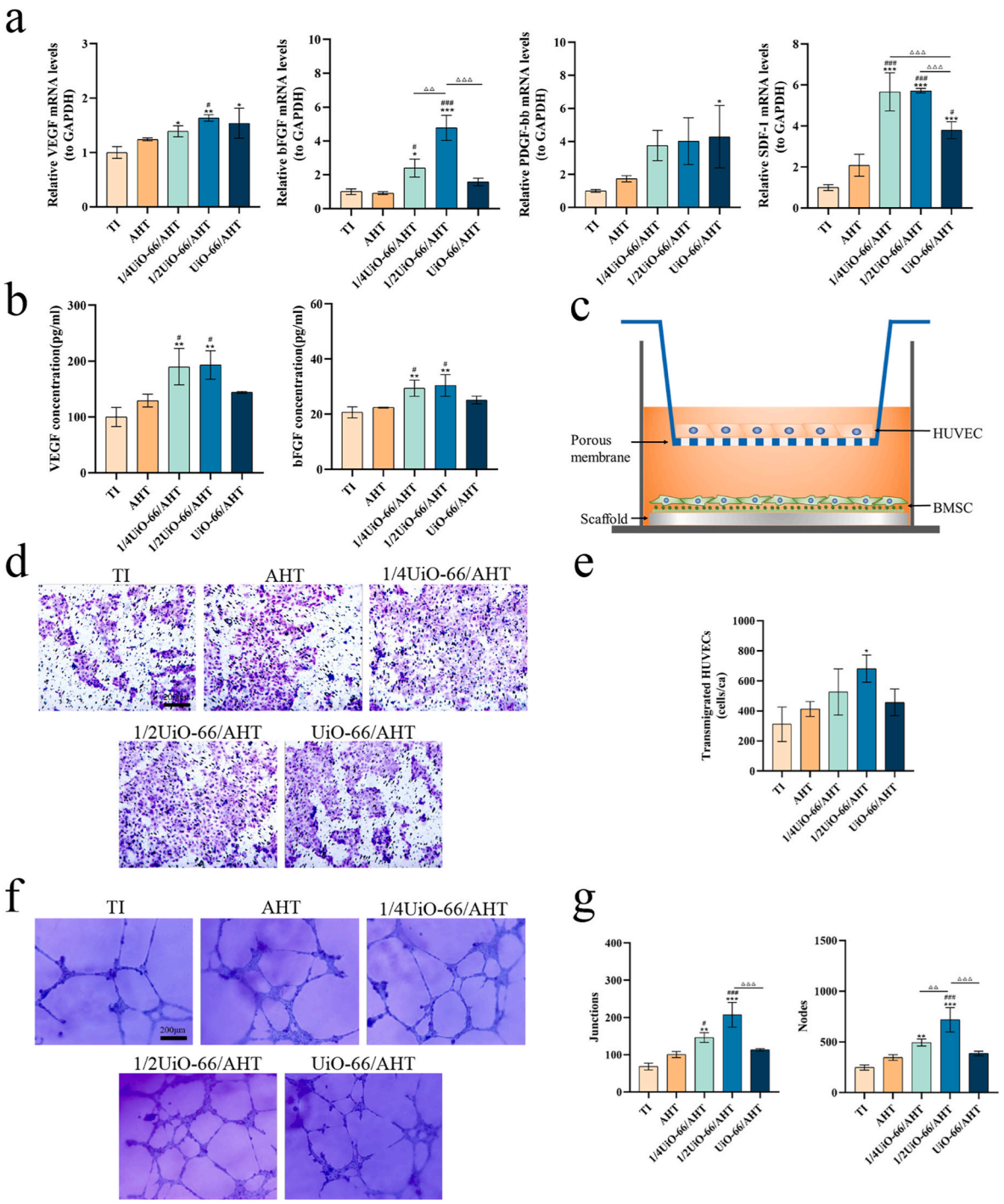

Fig. 8. In vitro angiogenic regulation of BMSCs on different scaffolds: (a) Relative angiogenesis-related mRNA expression of BMSCs; (b) Quantified analysis of VEGF and bFGF concentrations secreted by BMSCs in Elisa kit; (c) Schematic illustration of Scheme of BMSCs and HUVECs co-culture system; (d) Representative images of transmigrated HUVECs in co-culture systems; (e) Quantitative analysis for transmigrated HUVECs; (f) Representative images of tube formation in co-culture systems; (g) Quantitative analysis for tube formation; $^{*}p < 0.05$, $^{**}p < 0.01$, $^{***}p < 0.005$ compared with TI group, $^{\#}p < 0.05$, $^{\#\#}p < 0.01$, $^{\#\#\#}p < 0.005$ compared with AHT group, $^{\triangle}p < 0.05$, $^{\triangle\triangle}p < 0.01$, $^{\triangle\triangle\triangle}p < 0.005$.

Integrin, a family of adhesion proteins in endothelial cells, plays a significant role in mechanotransduction and the sensing of topography [104]. The nano-topography, such as nanotubes, has been shown to facilitate the clustering of integrin, leading to the reorganization of the cytoskeleton and activation of the PI3K/Akt/eNOS pathway [92,105,106]. Therefore, the scaffold with nano-topography could induce the upregulation of the phosphorylation of eNOS and the synthesis of NO to promote the angiogenic differentiation of ECs [107].

3.6. Communication between BMSCs and HUVEC mediated by scaffold

3.6.1. Osteogenic promotion of HUVECs mediated by scaffold

The mRNA expression and secretion level of paracrine factors of the Wnt and BMP family were first detected (Fig. 7a–b). The RT-PCR results displayed that the mRNA expression level of osteogenic factors in 1/4UiO-66/AHT and 1/2UiO-66/AHT were generally higher than that in TI and AHT groups ($p < 0.05$). The Elisa results confirmed a similar trend as well. To further assess the osteogenic regulatory effect of HUVECs inspired by scaffolds, the migrative situation and ALP activity of BMSCs co-cultivated with HUVECs in the transwell system were evaluated (Fig. 7d–g). The BMSCs in 1/4UiO-66/AHT and 1/2/UiO-66/AHT were observed to have significantly better transmembrane migration than the TI group ($p < 0.05$). As to ALP activity evaluation, the cells in 1/2UiO-66/AHT accumulated more ALP product than other groups ($p < 0.05$). Recent studies stressed the beneficial impact of EC-derived osteogenic factors in bone regeneration [26]. The Wnt/β-catenin signaling pathway is a crucial axis that significantly contributes to the maintenance, restoration, and regeneration of bone and cartilage homeostasis [108]. One notable member of this pathway is Wnt3a, which can be secreted by endothelial cells and is involved in the coordination of angiogenesis and osteogenesis [109,110]. According to reports, endothelial cell-derived Wnt3a has been found to enhance the early osteogenesis of co-cultured BMSCs [32]. The BMP family, which is widely expressed in the vasculature, acts as a regulatory factor and has a positive impact on

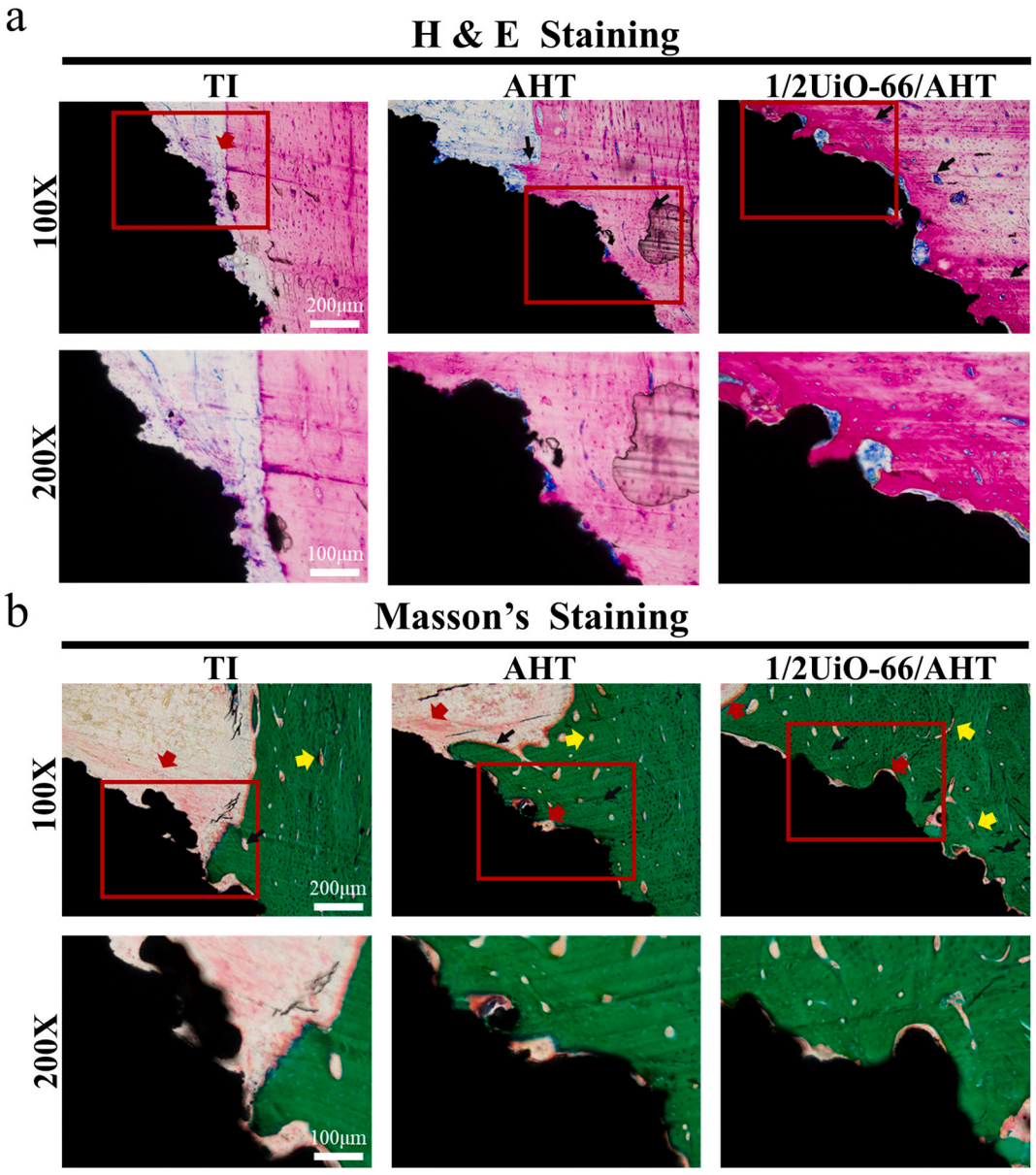

Fig. 9. Histological observation of osseointegration in vivo: (a) Representative H&E staining images, red arrow: newly formed but unmineralized bone (osteoid), black arrow: mineralized and matured bone; (b) Goldner's Trichrome staining images, red arrow: newly formed but unmineralized bone (osteoid), black arrow: mineralized and matured bone; yellow arrow: new vessels. (For interpretation of the references to colour in this figure legend, the reader is referred to the Web version of this article.)

bone mineralization and regeneration [111,112]. BMP2, the primary member of the BMP family, induces osteogenesis through the activation of Smads, as well as transcription factors like Runx2, and others [113]. These results indicated that the incorporation of UiO-66 modified nanostructures into titanium scaffolds, particularly at a 1/2UiO-66/AHT ratio, could significantly enhance the paracrine activity of HUVECs, thereby promoting osteogenesis through the activation of the Wnt and BMP signaling pathways.

3.6.2. Angiogenic promotion of BMSCs mediated by scaffold

The expression of angiogenic-related genes and secretion of paracrine factors of BMSCs were first evaluated. Compared to TI group, scaffolds with UiO-66 modified nanostructures generally improved the expression of VEGF, bFGF, bb-PDGF, and SDF-1 (Fig. 8a). The Elisa results further validate that BMCSs adhered to AHT with UiO-66 modification tend to secrete higher levels of VEGF and bFGF, particularly in the 1/4UiO-66/AHT and 1/2UiO-66/AHT groups (Fig. 8b) (see Fig. 9).

It is worth noting that MSC participated in neo-angiogenesis via paracrine effects, involving diverse angiogenic factors and cytokines [111]. For example, SDF-1 is one of the chemokines stimulating cell migration [114]. PDGF-bb is a chemotactic and mitogenic factor participating in the formation of type H blood vessels [115]. The HIF-1α/VEGF signaling pathway is considered an indispensable driving force for angiogenesis induction during bone regeneration [116]. bFGF is a wide-spectrum growth stimulant activating ECs proliferation, chemotaxis, and intercellular junction communication [117]. It has been proven that the secretion of angiogenic factors could be enhanced by single microstructured or nanostructured topography [21,118]. Our studies provide additional evidence supporting the synergistic impact of micro/nano hierarchical structures on the angiogenic paracrine activities of BMSCs.

The BMSCs were seeded on different scaffolds and co-cultured with HUVECs on the upper chambers (Fig. 8c). 1/2UiO-66/AHT displayed both the highest tube formation activity and migrative action (Fig. 8d–g). The aforementioned findings indicate that the incorporation of 1/2UiO-66/AHT has the potential to augment the paracrine communication between BMSCs and HUVECs, thereby facilitating enhanced angiogenic capabilities.

3.7. In vivo osteogenesis and angiogenesis of different peri-scaffolds

To further evaluate the combined effects of UiO-66 modified hierarchical micro/nano topography, 1/2UiO-66/AHT, which showed the best capability of enhancing osteogenesis, angiogenesis, and their coupling relationship in vitro experiments, was selected for further vivo studies. Both H&E and Goldner's trichrome staining images displayed that thicker and more mature bone contacted directly to the scaffold in the AHT and 1/2UiO-66/AHT group, confirming the higher levels of bone formation. Moreover, more new blood vessels were observed in 1/2UiO-66/AHT in comparison to the other two groups.

The immunohistochemistry staining of OCN and CD31, the marker of neo-bone tissue and blood vessels, was carried out and depicted (Fig. 10a) [32]. As we could see, both OCN or CD31 staining areas presented most in the 1/2UiO-66/AHT group, indicating the highest potential for osteogenesis and angiogenesis coupling promotion. In addition, it was observed that the presence of OCN, a recognized indicator of mature osteoblasts, was concentrated around the blood vessels across all experimental groups. This observation agreed with previous research suggesting that osteoprogenitors tend to localize around type H vessels, owing to the abundant supply of oxygen, nutrients, and cytokines provided by these vessels [115]. his phenomenon provides clear evidence that neo-vasculature has the ability to support bone

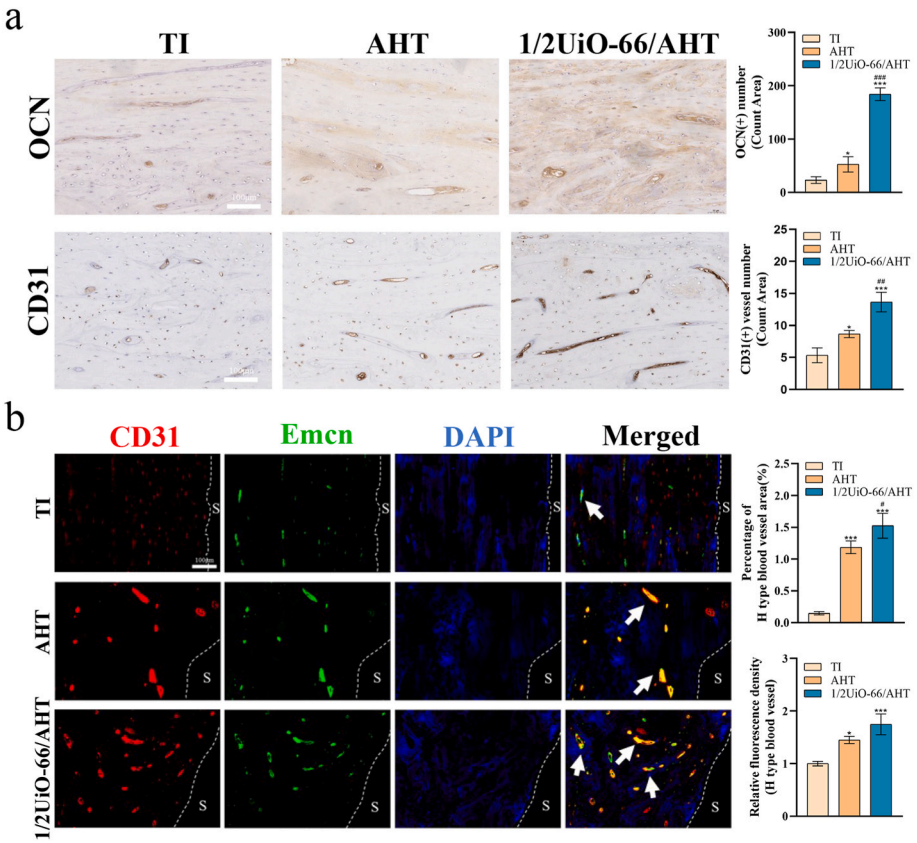

Fig. 10. Immunohistochemistry and immunofluorescence staining evaluation: (a) Representative immunohistochemistry staining images for OCN,CD31 and the colorimetric quantitative results, black triangle: blood vessel; (b) Representative immunofluorescence staining images for EMCN, CD31 and quantitative analysis of H type vessel, S:scaffold; $^{*}p < 0.05$, $^{**}p < 0.01$, $^{***}p < 0.005$ compared with TI group, $^{\#}p < 0.05$, $^{\#\#}p < 0.01$, $^{\#\#\#}p < 0.005$ compared with AHT group.

regeneration [119]. OCN, as a regulatory factor secreted by osteoblasts, also has a positive impact on vasculature [111]. Research has shown that OCN can enhance the functionality of ECs by upregulating NO and NF-κB signals through the PI3K/Akt/eNOS pathway [120].

It has been widely considered that the blood vessel in bone tissue with high expression of CD31 and EMCN could be subdivided into type H vessels while the one with low expression is subdivided into type L vessels [32]. Type H is regarded as a specific subtype of blood vessel grown in the area with dynamic bone metabolism regions, which suggests the tight coupling relationship between angiogenesis and osteogenesis [27,30,115]. Due to the unique characteristics of dual positive EMCN and CD31, the type H vessels were performed as yellowish areas in the images (Fig. 10b). It was difficult to observe yellowish areas in the pictures of the TI group. Oppositely, the yellowish areas representing type H vessels were visible in the AHT and more abundant in the 1/2UiO-66/AHT. The quantitative analysis provided confirmation of the visual observation that 1/2UiO-66/AHT exhibited the greatest enrichment of type H vessels among the three groups ($p < 0.05$). The in vivo experimental results validated the in vitro finding that the hierarchical micro/nano topographic structure modified by UiO-66 could facilitate coupling osteogenesis and angiogenesis in bone healing.

Chen et al. reported that scaffolds featuring nano-topographic structures exert a stimulating influence on the coupling relationship of angiogenesis and osteogenesis via cell-topography interaction [21]. Moreover, Hu et al. found that nanotubes, especially those with a diameter of 70 nm, had remarkable influences on the development of type H vessels via binding to integrin [33]. Zeng et al. developed a biomimetic hydrogel mixed micro/nano bioactive glass, which effectively accelerated vascularization and osteogenesis synergistically [121]. In this study, a novel biomimetic titanium scaffold with UiO-66 modified hierarchical micro/nano structure was constructed to provide a strategy to promote angiogenesis-osteogenesis coupling via integrin-mediated mechanotransduction. In comparison to other single micro or nano topographies, the hierarchical micro/nano structure exhibits notable advantages. The micro-scale structure enhances mechanical interlocking, while the nanoscale structure promotes protein absorption, cell adhesion, and mechanotransduction [90,122]. Furthermore, the additional modification of UiO-66 not only enhances the protein absorption capability of the scaffold but also creates a rod/crystal hybrid nanostructure that increases the disorder of the nanopattern and further stimulates osteogenic differentiation [55,94]. The enhanced protein capability resulting from the modification of nanostructures with UiO-66 reinforces the integrin-mediated mechanotransduction and activation of several downstream signaling pathways [40,123,124]. Eventually, the activated pathways exerted a positive effect on osteogenic differentiation of BMSCs, angiogenic differentiation of HUVEC, and the communication between them by enhancing paracrine behaviors [21,114].

4. Conclusion

In this work, a novel UiO-66 modified hierarchical micro/nano topographic structure on a 3D-printed titanium scaffold was successfully constructed. In comparison with TI, AHT, and other UiO-66/AHTs, 1/2UiO-66/AHT exhibited the best osteogenic and angiogenic induction as well as promotion of the intercellular communication between BMSCs and HUVECs by enhancing paracrine effects. This study provides a surface topography design by taking full advantage of the synergistic effect of the hierarchical topographic structure to achieve the coupling of osteogenesis and angiogenesis. This strategy holds promise for improving the biological inertness of titanium scaffolds and facilitating the successful integration of regenerated bone with the scaffold.

CRediT authorship contribution statement

Leyi Liu: Conceptualization, Methodology, Software, Data curation, Formal analysis, Writing - original draft, Writing - review & editing, contributed equally to this work, belonged to co-first author. **Jie Wu:** Conceptualization, Methodology, Software, Data curation, Formal analysis, Writing - review & editing, contributed equally to this work, belonged to co-first author. **Shiyu Lv:** Methodology, Data curation, Formal analysis, Writing - original draft, contributed equally to this work, belonged to co-first author, contributed equally to this work, belonged to co-first author. **Duoling Xu:** Methodology. **Shujun Li:** Investigation. **Wentao Hou:** Validation. **Chao Wang:** Supervision, Resources, Project administration, Writing - review & editing. **Dongsheng Yu:** Supervision, Funding acquisition, Project administration.

Declaration of competing interest

The authors declare that they have no known competing financial interests or personal relationships that could have appeared to influence the work reported in this paper.

Data availability

Data will be made available on request.

Acknowledgements

This work was supported by the National Natural Science Foundation of China (Nos. 82073378, 81974146), the Natural Science Foundation of Guangdong Province (2021A1515012399), Shenyang Talents program (RC200230), Special Funds for the Cultivation of Guangdong College Students' Scientific and Technological Innovation ("Climbing Program" Special Funds. pdjh2022b0012, pdjh2023a0004) and National Undergraduate Training Program for Innovation and Entrepreneurship (No. 202310824).

Appendix A. Supplementary data

Supplementary data to this article can be found online at https://doi.org/10.1016/j.mtbio.2023.100866.

References

[1] T. Tian, T. Zhang, Y. Lin, X. Cai, Vascularization in craniofacial bone tissue engineering, J. Dent. Res. 97 (2018) 969–976, https://doi.org/10.1177/0022034518767120.
[2] B.P. Kumar, V. Venkatesh, K.A. Kumar, B.Y. Yadav, S.R. Mohan, Mandibular reconstruction: overview, J. Maxillofac. Oral Surg. 15 (2016) 425–441, https://doi.org/10.1007/s12663-015-0766-5.
[3] B.M. Ferguson, A. Entezari, J. Fang, Q. Li, Optimal placement of fixation syste-m for scaffold-based mandibular reconstruction, J. Mech. Behav. Biomed. Mater. 126 (2022), 104855, https://doi.org/10.1016/j.jmbbm.2021.104855.
[4] A. Palmquist, M. Jolic, E. Hryha, F.A. Shah, Complex geometry and integrated macro-porosity: clinical applications of electron beam melting to fabricate bespoke bone-anchored implants, Acta Biomater. (2022), https://doi.org/10.1016/j.actbio.2022.06.002.
[5] S. Spriano, S. Yamaguchi, F. Baino, S. Ferraris, A critical review of multifunctional titanium surfaces: new frontiers for improving osseointegration and host response, avoiding bacteria contamination, Acta Biomater. 79 (2018) 1–22, https://doi.org/10.1016/j.actbio.2018.08.013.
[6] F. Trevisan, et al., Additive manufacturing of titanium alloys in the biomedical field: processes, properties and applications, J Appl Biomater Func 16 (2018) 57–67, https://doi.org/10.5301/jabfm.5000371.
[7] T.T. Oliveira, A.C. Reis, Fabrication of dental implants by the additive manufacturing method: a systematic review, J. Prosthet. Dent 122 (2019) 270–274, https://doi.org/10.1016/j.prosdent.2019.01.018.
[8] I. Mitra, et al., 3D Printing in alloy design to improve biocompatibility in metallic implants, Mater. Today 45 (2021) 20–34, https://doi.org/10.1016/j.mattod.2020.11.021.
[9] S. Jiang, et al., Synergistic effect of micro-nano-hybrid surfaces and Sr doping on the osteogenic and angiogenic capacity of hydroxyapatite bioceramics scaffolds, Int. J. Nanomed. 17 (2022) 783–797, https://doi.org/10.2147/IJN.S345357.
[10] R. Xu, et al., Micro-/nano-topography of selective laser melting titanium enhances adhesion and proliferation and regulates adhesion-related gene expressions of human gingival fibroblasts and human gingival epithelial cells, Int. J. Nanomed. 13 (2018) 5045–5057, https://doi.org/10.2147/IJN.S166661.

[11] J. Zhang, et al., Cell responses to titanium treated by a sandblast-free method for implant applications, Mater. Sci. Eng., C 78 (2017) 1187–1194, https://doi.org/10.1016/j.msec.2017.04.119.

[12] A. Jayasree, N.T. Raveendran, T. Guo, S. Ivanovski, K. Gulati, Electrochemically nano-engineered titanium: influence of dual micro-nanotopography of anisotropic nanop-ores on bioactivity and antimicrobial activity, Mater Today Adv 15 (2022).

[13] K. Gulati, H.J. Moon, T. Li, P.T. Sudheesh Kumar, S. Ivanovski, Titania nanopores with dual micro-/nano-topography for selective cellular bioactivity, Mater. Sci. Eng., C 91 (2018) 624–630, https://doi.org/10.1016/j.msec.2018.05.075.

[14] S. Maher, et al., Advancing of additive-manufactured titanium implants with bioinspir-ed micro- to nanotopographies, ACS Biomater. Sci. Eng. 7 (2021) 441–450, https://doi.org/10.1021/acsbiomaterials.0c01210.

[15] L. Bai, et al., A micro/nano-biomimetic coating on titanium orchestrates osteo/angio-gen-esis and osteoimmunomodulation for advanced osseointegration, Biomaterials 278 (2021), 121162, https://doi.org/10.1016/j.biomaterials.2021.121162.

[16] W. Zhang, et al., The synergistic effect of hierarchical micro/nano-topography and bioac-tive ions for enhanced osseointegration, Biomaterials 34 (2013) 3184–3195, https://doi.org/10.1016/j.biomaterials.2013.01.008.

[17] R.A. Gittens, R. Olivares-Navarrete, Z. Schwartz, B.D. Boyan, Implant osseointegration and the role of microroughness and nanostructures: lessons for spine implants, Acta Biomater. 10 (2014) 3363–3371, https://doi.org/10.1016/j.actbio.2014.03.037.

[18] B.S. Moon, S. Kim, H.E. Kim, T.S. Jang, Hierarchical micro-nano structured Ti6Al4V surface topography via two-step etching process for enhanced hydrophilicity and osteoblastic responses, Mater. Sci. Eng., C 73 (2017) 90–98, https://doi.org/10.1016/j.msec.2016.12.064.

[19] C.J. Deng, et al., Micro/nanometer-Structured scaffolds for regeneration of both cartilage and subchondral bone, Adv. Funct. Mater. 29 (2019). ARTN.

[20] N. Khosravi, R.S. DaCosta, J.E. Davies, New insights into spatio-temporal dynamics of mesenchymal progenitor cell ingress during peri-implant wound healing: provided by intravital imaging, Biomaterials 273 (2021).

[21] W. Chen, et al., Multilayered coating of titanium implants promotes coupled osteogenesis and angiogenesis in vitro and in vivo, Acta Biomater. 74 (2018) 489–504, https://doi.org/10.1016/j.actbio.2018.04.043.

[22] S.K. Ramasamy, et al., Blood flow controls bone vascular function and osteogenesis, Nat. Commun. 7 (2016), 13601, https://doi.org/10.1038/ncomms13601.

[23] J.Y. Ji, C.J. Wang, Z. Xiong, Y. Pang, W. Sun, 3D-printed scaffold with halloysite nanotubes laden as a sequential drug delivery system regulates vascularized bone tissue healing, Mater Today Adv 15 (2022).

[24] H. Liu, et al., Engineering 3D-printed strontium-titanium scaffold-integrated highly bioactive serum exosomes for critical bone defects by osteogenesis and angiogenesis, Acs Appl Mater Inter 15 (2023) 27486–27501, https://doi.org/10.1021/acsami.3c00898.

[25] Y. Li, et al., Tissue engineered neurovascularization strategies for craniofacial tissue regeneration, ACS Appl. Bio Mater. 5 (2022) 20–39, https://doi.org/10.1021/acsabm.1c00979.

[26] S. Zhu, et al., Endothelial cells produce angiocrine factors to regulate bone and cartilage via versatile mechanisms, Theranostics 10 (2020) 5957–5965, https://doi.org/10.7150/thno.45422.

[27] J. Zhang, J. Pan, W. Jing, Motivating role of type H vessels in bone regeneration, Cell Prolif. 53 (2020), e12874, https://doi.org/10.1111/cpr.12874.

[28] B. Huang, et al., Osteoblasts secrete Cxcl9 to regulate angiogenesis in bone, Nat. Commun. 7 (2016), 13885, https://doi.org/10.1038/ncomms13885.

[29] S.Y. Sun, et al., Osteogenic differentiated human bone marrow stem cells contribute to sprouting angiogenesis deceleration via paracrine excreted IGFBP7, Adv. Mater. Interfac. 9 (2022), https://doi.org/10.1002/admi.202201719.

[30] A.P. Kusumbe, S.K. Ramasamy, R.H. Adams, Coupling of angiogenesis and osteogenesis by a specific vessel subtype in bone, Nature 507 (2014) 323–328, https://doi.org/10.1038/nature13145.

[31] S.K. Ramasamy, A.P. Kusumbe, L. Wang, R.H. Adams, Endothelial Notch activ-ity promotes angiogenesis and osteogenesis in bone, Nature 507 (2014) 376–380, https://doi.org/10.1038/nature13146.

[32] W. Chen, et al., An improved osseointegration of metal implants by pitavastatin loaded multilayer films with osteogenic and angiogenic properties, Biomaterials 280 (2022), 121260, https://doi.org/10.1016/j.biomaterials.2021.121260.

[33] X. Hu, et al., Effects of material nano-topography on the angiogenesis of type H vessels: size dependence, cell heterogeneity and intercellular communication, Biomater. Adv. 147 (2023), 213307, https://doi.org/10.1016/j.bioadv.2023.213307.

[34] Y. Yang, et al., Biomimetic, stiff, and adhesive periosteum with osteogenic-angiogenic coupling effect for bone regeneration, Small 17 (2021), e2006598, https://doi.org/10.1002/smll.202006598.

[35] N. Singh, S. Qutub, N.M. Khashab, Biocompatibility and biodegradability of metal organic frameworks for biomedical applications, J. Mater. Chem. B 9 (2021) 5925–5934, https://doi.org/10.1039/d1tb01044a.

[36] F. Oroojalian, et al., Current trends in stimuli-responsive nanotheranostics based on met-al-organic frameworks for cancer therapy, Mater. Today 57 (2022) 192–224, https://doi.org/10.1016/j.mattod.2022.05.024.

[37] J. Yang, Y.W. Yang, Metal-organic frameworks for biomedical applications, Small 16 (2020), e1906846, https://doi.org/10.1002/smll.201906846.

[38] Y. Zhang, et al., Functionally tailored metal-organic framework coatings for mediating Ti implant osseointegration, Adv. Sci. (2023), e2303958, https://doi.org/10.1002/advs.202303958.

[39] L. Wang, X. You, L. Zhang, C. Zhang, W. Zou, Mechanical regulation of bone remodeling, Bone Res 10 (2022) 16, https://doi.org/10.1038/s41413-022-00190-4.

[40] X. Chen, et al., Scaffold structural microenvironmental cues to guide tissue regeneration in bone tissue applications, Nanomaterials 8 (2018), https://doi.org/10.3390/nano8110960.

[41] M.A. Fardjahromi, et al., Metal-organic framework-based nanomaterials for bone tissue engineering and wound healing, Mater. Today Chem. 23 (2022).

[42] W. Wang, Y.Z. Xiong, R.L. Zhao, X. Li, W.T. Jia, A novel hierarchical biofunctionalized 3D-printed porous Ti6Al4V scaffold with enhanced osteoporotic osseointegration through osteoimmunomodulation, J. Nanobiotechnol. 20 (2022).

[43] S.M. Dehnavi, M. Barjasteh, S.A. Seyedkhani, S.Y. Rahnamaee, R. Bagheri, A novel silver-based metal-organic framework incorporated into nanofibrous chitosan coatings for bone tissue implants, Int. J. Pharm. (Amst.) 640 (2023).

[44] Y.H. Si, H.Y. Liu, H.Y. Yu, X.Z. Jiang, D.B. Sun, MOF-derived CuO@ZnO modified titanium implant for synergistic antibacterial ability, osteogenesis and angiogenesis, Colloids Surf., B 219 (2022), 112840.

[45] A. Farboudi, et al., UiO-66 metal organic framework nanoparticles loaded carboxymeth-yl chitosan/poly ethylene oxide/polyurethane core-shell nanofibers for controlled release of doxorubicin and folic acid, Int. J. Biol. Macromol. 150 (2020) 178–188, https://doi.org/10.1016/j.ijbiomac.2020.02.067.

[46] S. Zhang, X. Pei, H.L. Gao, S. Chen, J. Wang, Metal-organic framework-based nanomaterials for biomedical applications, Chin. Chem. Lett. 31 (2020) 1060–1070, https://doi.org/10.1016/j.cclet.2019.11.036.

[47] Y. Sun, et al., Metal-organic framework nanocarriers for drug delivery in biomedical applications, Nano-Micro Lett. 12 (2020) 103, https://doi.org/10.1007/s40820-020-00423-3.

[48] W.A. El-Mehalmey, et al., Nine days extended release of adenosine from biocompatible MOFs under biologically relevant conditions, Biomater. Sci. 10 (2022) 1342–1351, https://doi.org/10.1039/d1bm01519b.

[49] J. Winarta, et al., A decade of UiO-66 research: a historic review of dynamic structure, synthesis mechanisms, and characterization techniques of an archetypal metal-organic framework, Cryst. Growth Des. 20 (2020) 1347–1362, https://doi.org/10.1021/acs.cgd.9b00955.

[50] I. Abanades Lazaro, et al., Selective surface PEGylation of UiO-66 nanoparticles for enhanced stability, cell uptake, and pH-responsive drug delivery, Chem 2 (2017) 561–578, https://doi.org/10.1016/j.chempr.2017.02.005.

[51] M.N. Goda, H.N. Abdelhamid, A.A. Said, Zirconium oxide sulfate-carbon (ZrOSO4@C) derived from carbonized UiO-66 for selective production of dimethyl ether, Acs Appl Mater Inter 12 (2020) 646–653, https://doi.org/10.1021/acsami.9b17520.

[52] I. Abanades Lazaro, C.J.R. Wells, R.S. Forgan, Multivariate modulation of the Zr MOF UiO-66 for defect-controlled combination anticancer drug delivery, Angew Chem. Int. Ed. Engl. 59 (2020) 5211–5217, https://doi.org/10.1002/anie.201915848.

[53] Z. Xu, et al., A metal-organic framework-based immunomodulatory nanoplatform for anti-atherosclerosis treatment, J. Contr. Release 354 (2023) 615–625, https://doi.org/10.1016/j.jconrel.2023.01.024.

[54] A. Karakecili, et al., UiO-66 metal-organic framework as a double actor in chitosan sc-affolds: antibiotic carrier and osteogenesis promoter, Biomater. Adv. 136 (2022), 212757, https://doi.org/10.1016/j.bioadv.2022.212757.

[55] T. Katayama, S. Tanaka, T. Tsuruoka, K. Nagahama, Two-dimensional metal-organ-ic framework-based cellular scaffolds with high protein adsorption, retention, and replenishment capabilities, ACS Appl. Mater. Interfaces 14 (2022) 34443–34454, https://doi.org/10.1021/acsami.2c08677.

[56] Z.L. Mensinger, B.L. Cook, E.L. Wilson, Adsorption of amyloid beta peptide by metal-organic frameworks, ACS Omega 5 (2020) 32969–32974, https://doi.org/10.1021/acsomega.0c04019.

[57] J. Barberi, S. Spriano, Titanium and protein adsorption: an overview of mechanisms and effects of surface features, Materials 14 (2021), https://doi.org/10.3390/ma14071590.

[58] C. Wang, et al., Large-pore-size Ti6Al4V scaffolds with different pore structures for vascularized bone regeneration, Mater. Sci. Eng., C 131 (2021), 112499, https://doi.org/10.1016/j.msec.2021.112499.

[59] N. Chosa, M. Taira, S. Saitoh, N. Sato, Y. Araki, Characterization of apatite formed on alkaline-heat-treated Ti, J. Dent. Res. 83 (2004) 465–469, https://doi.org/10.1177/154405910408300606.

[60] B. Yan, et al., Constructing fluorine-doped Zr-MOF films on titanium for antibacteria, anti-inflammation, and osteogenesis, Biomater. Adv. 134 (2022), 112699, https://doi.org/10.1016/j.msec.2022.112699.

[61] X. Li, et al., Enhanced bone regenerative properties of calcium phosphate ceramic granules in rabbit posterolateral spinal fusion through a reduction of grain size, Bioact. Mater. 11 (2022) 90–106, https://doi.org/10.1016/j.bioactmat.2021.10.006.

[62] X. Li, et al., Fabrication and properties of Ca-P bioceramic spherical granules with in-terconnected porous structure, ACS Biomater. Sci. Eng. 3 (2017) 1557–1566, https://doi.org/10.1021/acsbiomaterials.7b00232.

[63] S. Ponader, et al., Effects of topographical surface modifications of electron beam melted Ti-6Al-4V titanium on human fetal osteoblasts, J. Biomed. Mater. Res. 84 (2008) 1111–1119, https://doi.org/10.1002/jbm.a.31540.

[64] Y.T. Han, et al., Facile synthesis of morphology and size-controlled zirconium metal-organic framework UiO-66: the role of hydrofluoric acid in crystallization, CrystEngComm 17 (2015) 6434–6440, https://doi.org/10.1039/c5ce00729a.

[65] C.W. Abney, et al., Topotactic transformations of metal organic frameworks to highly porous and stable inorganic sorbents for efficient radionuclide

sequestration, Chem. Mater. 26 (2014) 5231–5243, https://doi.org/10.1021/cm501894h.
[66] X. Zhang, et al., Enhanced osseointegration of porous titanium modified with zeolitic imidazolate framework-8, ACS Appl. Mater. Interfaces 9 (2017) 25171–25183, https://doi.org/10.1021/acsami.7b07800.
[67] E. Martines, et al., Superhydrophobicity and superhydrophilicity of regular nanopatterns, Nano Lett. 5 (2005) 2097–2103, https://doi.org/10.1021/nl051435t.
[68] J. Zhong, et al., Effect of acid-alkali treatment on serum protein adsorption and bacterial adhesion to porous titanium, J. Mater. Sci. Mater. Med. 33 (2022) 20, https://doi.org/10.1007/s10856-022-06646-7.
[69] X. Zhang, et al., Surface immobilization of heparin and chitosan on titanium to improve hemocompatibility and antibacterial activities, Colloids Surf. B Biointerfaces 172 (2018) 338–345, https://doi.org/10.1016/j.colsurfb.2018.08.060.
[70] X.F. Ma, et al., When MOFs meet wood: from opportunities toward applications, Chem 8 (2022) 2342–2361, https://doi.org/10.1016/j.chempr.2022.06.016.
[71] W.S.Y. Teng, et al., Iodine immobilized metal-organic framework for NIR-triggered antibacterial therapy on orthopedic implants, Small 17 (2021).
[72] L.M. Yu, et al., Simultaneous adsorption and determination of bisphenol compounds in water medium with a Zr(IV)-based metal-organic framework, Microchim. Acta 188 (2021).
[73] C.G. Dodo, P.M. Senna, W. Custodio, A.F. Paes Leme, A.A. Del Bel Cury, Proteome analysis of the plasma protein layer adsorbed to a rough titanium surface, Biofouling 29 (2013) 549–557, https://doi.org/10.1080/08927014.2013.787416.
[74] B. Ren, et al., Improved osseointegration of 3D printed Ti-6Al-4V implant with a hierarchical micro/nano surface topography: an in vitro and in vivo study, Mater. Sci. Eng., C 118 (2021), 111505, https://doi.org/10.1016/j.msec.2020.111505.
[75] M. Nakamura, et al., Surface free energy predominates in cell adhesion to hydroxyapatite through wettability, Mat Sci Eng C-Mater 62 (2016) 283–292, https://doi.org/10.1016/j.msec.2016.01.037.
[76] R. Zhou, et al., Structure, MC3T3-E1 cell response, and osseointegration of macroporous titanium implants covered by a bioactive microarc oxidation coating with microporous structure, ACS Appl. Mater. Interfaces 6 (2014) 4797–4811, https://doi.org/10.1021/am405680d.
[77] C. Liu, et al., Bovine serum albumin adsorption in mesoporous titanium dioxide: pore size and pore chemistry effect, Langmuir 32 (2016) 3995–4003, https://doi.org/10.1021/acs.langmuir.5b04496.
[78] B. Wu, Y. Tang, K. Wang, X. Zhou, L. Xiang, Nanostructured titanium implant surface facilitating osseointegration from protein adsorption to osteogenesis: the example of TiO(2) NTAs, Int. J. Nanomed. 17 (2022) 1865–1879, https://doi.org/10.2147/IJN.S362720.
[79] H.P. Felgueiras, et al., Bone tissue response induced by bioactive polymer functionalized Ti6Al4V surfaces: in vitro and in vivo study, J. Colloid Interface Sci. 491 (2017) 44–54, https://doi.org/10.1016/j.jcis.2016.12.023.
[80] S. Bauer, P. Schmuki, K. von der Mark, J. Park, Engineering biocompatible implant surfaces Part I: materials and surfaces, Prog. Mater. Sci. 58 (2013) 261–326, https://doi.org/10.1016/j.pmatsci.2012.09.001.
[81] M. Griffin, R. Palgrave, V.G. Baldovino-Medrano, P.E. Butler, D.M. Kalaskar, Argon plasma improves the tissue integration and angiogenesis of subcutaneous implant-s by modifying surface chemistry and topography, Int. J. Nanomed. 13 (2018) 6123–6141, https://doi.org/10.2147/IJN.S167637.
[82] X. Fu, et al., Effects of nanotopography regulation and silicon doping on angiogenic and osteogenic activities of hydroxyapatite coating on titanium implant, Int. J. Nanomed. 15 (2020) 4171–4189, https://doi.org/10.2147/IJN.S252936.
[83] M.H. Wu, et al., Bioinspired redwood-like scaffolds coordinated by in situ-generated silica-containing hybrid nanocoatings promote angiogenesis and osteogenesis both in vitro and in vivo, Adv. Healthcare Mater. 10 (2021).
[84] X.M. Gao, et al., Nanoscale zeolitic imidazolate framework-8 activator of canonical MAPK signaling for bone repair, Acs Appl Mater Inter 13 (2021) 97–111, https://doi.org/10.1021/acsami.0c15945.
[85] K. Xiong, et al., Enhanced bovine serum albumin absorption on the N-hydroxysuccinimide activated graphene oxide and its corresponding cell affinity, Mater. Sci. Eng., C 81 (2017) 386–392, https://doi.org/10.1016/j.msec.2017.08.044.
[86] K.A. Kilian, B. Bugarija, B.T. Lahn, M. Mrksich, Geometric cues for directing the differentiation of mesenchymal stem cells, Proc. Natl. Acad. Sci. U.S.A. 107 (2010) 4872–4877, https://doi.org/10.1073/pnas.0903269107.
[87] K.S. Brammer, C.J. Frandsen, S. Jin, TiO2 nanotubes for bone regeneration, Trends Biotechnol. 30 (2012) 315–322, https://doi.org/10.1016/j.tibtech.2012.02.005.
[88] H.Y. Niu, et al., Surface topography regulates osteogenic differentiation of MSCs vi-a crosstalk between FAK/MAPK and ILK/beta-Catenin pathways in a hierarchically P-orous environment, ACS Biomater. Sci. Eng. 3 (2017) 3161–3175, https://doi.org/10.1021/acsbiomaterials.7b00315.
[89] S. Dobbenga, L.E. Fratila-Apachitei, A.A. Zadpoor, Nanopattern-induced osteogeni-c differentiation of stem cells - a systematic review, Acta Biomater. 46 (2016) 3–14, https://doi.org/10.1016/j.actbio.2016.09.031.
[90] Q. Gao, et al., mTORC2 regulates hierarchical micro/nano topography-induced osteogenic differentiation via promoting cell adhesion and cytoskeletal polymerization, J. Cell Mol. Med. 25 (2021) 6695–6708, https://doi.org/10.1111/jcmm.16672.
[91] C. Li, et al., In vitro bioactivity and biocompatibility of bio-inspired Ti-6Al-4V alloy surfaces modified by combined laser micro/nano structuring, Molecules 25 (2020), https://doi.org/10.3390/molecules25071494.
[92] A.M. Gomes, D.F. da Silva, F.J. Bezerra, W.F. Zambuzzi, Nanohydroxyapatite-coated titanium surface increases vascular endothelial cells distinct signaling responding to high glucose concentration, J. Funct. Biomater. 14 (2023), https://doi.org/10.3390/jfb14040188.
[93] F.J. Zhao, et al., Periosteum structure/function-mimicking bioactive scaffolds with piezoelectric/chem/nano signals for critical-sized bone regeneration, Chem. Eng. J. 402 (2020), 126203.
[94] M.J. Dalby, et al., The control of human mesenchymal cell differentiation using nanoscale symmetry and disorder, Nat. Mater. 6 (2007) 997–1003, https://doi.org/10.1038/nmat2013.
[95] C. Allan, et al., Osteoblast response to disordered nanotopography, J. Tissue Eng. 9 (2018), 2041731418784098, https://doi.org/10.1177/2041731418784098.
[96] E. Kingham, K. White, N. Gadegaard, M.J. Dalby, R.O. Oreffo, Nanotopographical cues augment mesenchymal differentiation of human embryonic stem cells, Small 9 (2013) 2140–2151, https://doi.org/10.1002/smll.201202340.
[97] C.F. Natale, J. Lafaurie-Janvore, M. Ventre, A. Babataheri, A.I. Barakat, Focal adhesion clustering drives endothelial cell morphology on patterned surfaces, J. R. Soc. Interface 16 (2019), 20190263, https://doi.org/10.1098/rsif.2019.0263.
[98] F. De Smet, I. Segura, K. De Bock, P.J. Hohensinner, P. Carmeliet, Mechanisms of vessel branching: filopodia on endothelial tip cells lead the way, Arterioscler. Thromb. Vasc. Biol. 29 (2009) 639–649, https://doi.org/10.1161/ATVBAHA.109.185165.
[99] P. Ucla, et al., Dynamics of endothelial engagement and filopodia formation in complex 3D microscaffolds, Int. J. Mol. Sci. 23 (2022), https://doi.org/10.3390/ijms23052415.
[100] R.S. Fischer, P.Y. Lam, A. Huttenlocher, C.M. Waterman, Filopodia and focal adhesions: an integrated system driving branching morphogenesis in neuronal pathfinding and angiogenesis, Dev. Biol. 451 (2019) 86–95, https://doi.org/10.1016/j.ydbio.2018.08.015.
[101] M. Kretschmer, D. Rudiger, S. Zahler, Mechanical aspects of angiogenesis, Cancers 13 (2021), https://doi.org/10.3390/cancers13194987.
[102] T. Lammermann, M. Sixt, Mechanical modes of 'amoeboid' cell migration, Curr. Opin. Cell Biol. 21 (2009) 636–644, https://doi.org/10.1016/j.ceb.2009.05.003.
[103] Z. Tang, et al., Microconvex dot-featured silk fibroin films for promoting human umbilical vein endothelial cell angiogenesis via enhancing the expression of bFGF and VEGF, ACS Biomater. Sci. Eng. 7 (2021) 2420–2429, https://doi.org/10.1021/acsbiomaterials.0c01647.
[104] C.J. Avraamides, B. Garmy-Susini, J.A. Varner, Integrins in angiogenesis and lymphangiogenesis, Nat. Rev. Cancer 8 (2008) 604–617, https://doi.org/10.1038/nrc2353.
[105] E. Beltran-Partida, et al., Improved in vitro angiogenic behavior on anodized titanium dioxide nanotubes, J. Nanobiotechnol. 15 (2017) 10, https://doi.org/10.1186/s12951-017-0247-8.
[106] J. Chen, R. Crawford, C. Chen, Y. Xiao, The key regulatory roles of the PI3K/akt signaling pathway in the functionalities of mesenchymal stem cells and applications in tissue regeneration, Tissue Eng. Part B-Re 19 (2013) 516–528, https://doi.org/10.1089/ten.teb.2012.0672.
[107] L. Peng, et al., Whole genome expression analysis reveals differential effects of TiO2 nanotubes on vascular cells, Nano Lett. 10 (2010) 143–148, https://doi.org/10.1021/nl903043z.
[108] Y. Chu, et al., beta-catenin mediates fluoride-induced aberrant osteoblasts activity and osteogenesis, Environ. Pollut. 265 (2020), 114734, https://doi.org/10.1016/j.envpol.2020.114734.
[109] H. Yamamoto, et al., The apical and basolateral secretion of Wnt11 and Wnt3a in polarized epithelial cells is regulated by different mechanisms, J. Cell Sci. 126 (2013) 2931–2943, https://doi.org/10.1242/jcs.126052.
[110] J. Shen, et al., EGFL6 regulates angiogenesis and osteogenesis in distraction osteogenesis via Wnt/beta-catenin signaling, Stem Cell Res. Ther. 12 (2021) 415, https://doi.org/10.1186/s13287-021-02487-3.
[111] M. Chen, et al., Skeleton-vasculature chain reaction: a novel insight into the mystery of homeostasis, Bone Res 9 (2021).
[112] Y. Wei, et al., Individualized plasticity autograft mimic with efficient bioactivity inducing osteogenesis, Int. J. Oral Sci. 13 (2021).
[113] V. Rosen, BMP2 signaling in bone development and repair, Cytokine Growth Factor Rev. 20 (2009) 475–480, https://doi.org/10.1016/j.cytogfr.2009.10.018.
[114] H. Qi, et al., Co-culture of BMSCs and HUVECs with simvastatin-loaded gelatin nanosphere/chitosan coating on Mg alloy for osteogenic differentiation and vasculogenesis, Int. J. Biol. Macromol. 193 (2021) 2021–2028, https://doi.org/10.1016/j.ijbiomac.2021.11.032.
[115] Y. Peng, S. Wu, Y. Li, J.L. Crane, Type H blood vessels in bone modeling and remodeling, Theranostics 10 (2020) 426–436, https://doi.org/10.7150/thno.34126.
[116] R.C. Riddle, R. Khatri, E. Schipani, T.L. Clemens, Role of hypoxia-inducible factor-1alpha in angiogenic-osteogenic coupling, J. Mol. Med. (Berl.) 87 (2009) 583–590, https://doi.org/10.1007/s00109-009-0477-9.
[117] A. Novais, E. Chatzopoulou, C. Chaussain, C. Gorin, The potential of FGF-2 in craniofacial bone tissue engineering: a review, Cells 10 (2021), https://doi.org/10.3390/cells10040932.
[118] A.L. Raines, et al., Regulation of angiogenesis during osseointegration by titanium sur-face microstructure and energy, Biomaterials 31 (2010) 4909–4917, https://doi.org/10.1016/j.biomaterials.2010.02.071.

[119] T. Xu, et al., Electrosprayed regeneration-enhancer-element microspheres power osteogenesis and angiogenesis coupling, Small 18 (2022), e2205695, https://doi.org/10.1002/smll.202205695.
[120] A. Patti, L. Gennari, D. Merlotti, F. Dotta, R. Nuti, Endocrine actions of osteocalcin, Internet J. Endocrinol. (2013), 846480, https://doi.org/10.1155/2013/846480(2013).
[121] Z. Yang, et al., Self-adhesive hydrogel biomimetic periosteum to promote critical-size bone defect repair via synergistic osteogenesis and angiogenesis, ACS Appl. Mater. Interfaces 14 (2022) 36395–36410, https://doi.org/10.1021/acsami.2c08400.
[122] H. Zheng, et al., Hierarchical micro-nano topography promotes cell adhesion and osteogenic differentiation via integrin alpha2-PI3K-akt signaling Axis, Front. Bioeng. Biotechnol. 8 (2020) 463, https://doi.org/10.3389/fbioe.2020.00463.
[123] J. Flournoy, S. Ashkanani, Y. Chen, Mechanical regulation of signal transduction in angiogenesis, Front. Cell Dev. Biol. 10 (2022), 933474, https://doi.org/10.3389/fcell.2022.933474.
[124] E.N. Mpoyi, et al., Protein adsorption as a key mediator in the nanotopographical control of cell behavior, ACS Nano 10 (2016) 6638–6647, https://doi.org/10.1021/acsnano.6b01649.